UNIVERSIDADE ESTADUAL PAULISTA
"JÚLIO DE MESQUITA FILHO"
INSTITUTO DE GEOCIÊNCIAS E CIÊNCIAS EXATAS

Trabalho de Conclusão de Curso

Curso de Graduação em Física

# STUDY ON THE PHYSICAL PROPERTIES OF MOLECULAR SYSTEMS WITH STRONG ELECTRONIC CORRELATION EFFECTS

Lucca Sbrissa de Souza

Prof. Dr. Mariano de Souza

Rio Claro (SP)

2025

UNIVERSIDADE ESTADUAL PAULISTA

Instituto de Geociências e Ciências Exatas

Câmpus de Rio Claro

Lucca Sbrissa de Souza

# STUDY ON THE PHYSICAL PROPERTIES OF MOLECULAR SYSTEMS WITH STRONG ELECTRONIC CORRELATION EFFECTS

Trabalho de Conclusão de Curso apresentado ao Instituto de Geociências e Ciências Exatas - Câmpus de Rio Claro, da Universidade Estadual Paulista Júlio de Mesquita Filho, para obtenção do grau de Bacharel em Física.

Rio Claro (SP)

2025

S729s

Souza, Lucca Sbrissa de
Study on the physical properties of molecular systems with strong electronic correlation effects / Lucca Sbrissa de Souza. -- Rio Claro, 2025
50 p. : il., fotos

Trabalho de conclusão de curso (Bacharelado - Física) - Universidade Estadual Paulista (UNESP), Instituto de Geociências e Ciências Exatas, Rio Claro
Orientador: Prof. Mariano de Souza

1. Condutores Moleculares. 2. Correlação eletrônica. 3. ordenamento de cargas. 4. Modelo de Hubbard. I. Título.

Sistema de geração automática de fichas catalográficas da Unesp. Dados fornecidos pelo autor(a).

Lucca Sbrissa de Souza

# STUDY ON THE PHYSICAL PROPERTIES OF MOLECULAR SYSTEMS WITH STRONG ELECTRONIC CORRELATION EFFECTS

Trabalho de Conclusão de Curso apresentado ao Instituto de Geociências e Ciências Exatas - Câmpus de Rio Claro, da Universidade Estadual Paulista Júlio de Mesquita Filho, para obtenção do grau de Bacharel em Física.

Comissão Examinadora

Prof. Dr. Mariano de Souza

Prof. Dr. Leandro Bufaiçal

Prof. Dr. Adriano José Galvani Otuka

Rio Claro, 11 de Novembro de 2025.

Assinatura do aluno

Assinatura do orientador

**Acknowledgements**

First, I would like to extend my gratitude to Professor Mariano de Souza for welcoming me so warmly into the Solid State Physics group during the pandemic period, without ever seeing me in person, for always supporting and encouraging me to do Science, and mainly for never stopping believing in me, even when I couldn't. The unique orientation provided by Professor Mariano allowed me to grow not only as an academic but mostly as a person. I feel deeply honored every day for being part of this group and for sharing moments of knowledge and happiness with you, Professor. For me, it is really inspiring and a real privilege to have you as an advisor. I would also like to thank Dr. Lucas Squillante for all the support, for helping me with technical issues, but mostly for all the advice that extends beyond Physics.

I would like to thank all my family, but especially my Mom Rita and my Dad Sandro, for always providing everything necessary for my development, for always respecting my choices, and especially for always prioritizing my education.

To Samuel, Gustavo, Matheus, Júlia, Kauã, and Lincon, thanks for making the Solid State Physics group experience feel like a family environment. Especially for Samuel and Gustavo, I thank you for sharing a house with me for almost three years, and mainly for helping me during the most difficult period of my life. I will always consider both of you as real brothers, who my academic life introduced me to.

I also would like to thank the financial support, i.e., scholarships, provided by PIBIC Conselho Nacional de Desenvolvimento Científico e Tecnológico (CNPq) during two years of undergraduate studies.

**Abstract**

Strong electronic correlation effects have attracted the attention of the scientific community for decades due to their fundamental character. The molecular conductors of the $(TMTTF)_2X$ family, where TMTTF is the tetramethyltetrathiafulvalene molecule and $X$ is a counter-anion, exhibit a series of exotic phases of matter that emerge from strong electronic correlation, such as Mott insulators, the charge-ordered phase, and antiferromagnetic ground states, for instance. The variation of temperature, hydrostatic pressure, and the counter-anion species can modify the physical properties of these systems. The main goal of this work is to present a brief discussion of these phases, the physical mechanisms involved in their transitions, and the experimental aspects of low temperature Physics.
Keywords: Molecular Conductors, Hubbard Model, Electronic Correlation, Charge-Ordering

**Resumo**

Os efeitos de forte correlação eletrônica têm atraído a atenção da comunidade científica há décadas devido às consequências fundamentais apresentadas por eles. Os condutores moleculares da família $(TMTTF)_2X$, onde TMTTF é a molécula de tetrametiltetratiafuvaleno e $X$ é um contra ânion, exibem uma série de fases exóticas da matéria que emergem a partir das correlações eletrônicas, como os isolantes de Mott, a fase de carga ordenada e *ground states* antiferromagnéticos, por exemplo. A variação da temperatura, da pressão hidrostática e a espécie dos contra-ânions modificam as propriedades físicas destes sistemas. O objetivo principal deste trabalho é promover uma breve discussão sobre tais fases, os mecanismos físicos envolvidos em suas transições e aspectos experimentais para explorar a Física de baixas temperaturas.
Palavras-chave: Condutores Moleculares, Modelo de Hubbard, Correlação eletrônica, ordenamento de carga

Table of contents


1 INTRODUCTION . . . . . 9

2 STRUCTURAL ASPECTS OF THE FABRE-BECHGAARD SALTS . . . . . 11

2.1 Phase transitions and thermal expansion measurements . . . . . 12

3 THE ELECTRONS LOCALIZATION AND THE EMERGENCE OF AN INSULATING PHASE . . . . . 15

4 THE INHOMOGENEOUS REARRANGEMENT OF CHARGES . . . . . 18

4.1 Lattice effects in the charge-ordering phase transition . . . . . 20

5 MAGNETIC GROUND STATES OF THE FABRE SALTS . 26

5.1 The so-called spin-Peierls transition . . . . . 27

6 EXPERIMENTAL ASPECTS OF LOW TEMPERATURE PHYSICS . . . . . 30

6.1 Cooling by expansion: Teslatron-PT principle of work . . . . . 31

6.2 Cleaning up of the Zeolite trap and $^4$He circulation lines . . . . 32

6.3 Preparation for system cooling: the circulation of high purity $^4$He . . . . . 35

6.4 Decreasing the temperature . . . . . 36

6.5 Adjusting the needle valve pressure . . . . . 37

6.6 Attachment of electrical contacts in samples of interest . . . . . 37

6.7 Achieving high quality vacuum . . . . . 40

6.7.1 On the principle of work of vacuum pumps . . . . . 40

7 CONCLUSIONS AND OUTLOOKS . . . . . 47

REFERENCES . . . . . 48

# 1 Introduction

Since the discovery of electrons by J. J. Thomson in 1897, they have been one of the main objects of study in all fields of Science due to their fundamental nature, giving rise to research topics related to the electrical properties of materials. In 1911, K. Onnes discovered superconductivity using a Mercury wire at temperature $T = 4.2\,\mathrm{K}$ [1] cooled with liquefied Helium. With the observation of the abrupt decrease in electrical resistivity at the critical temperature $T_\mathrm{C}$, the search for materials with higher $T_\mathrm{C}$'s became a very popular topic in Physics and Chemistry. In the decade of 1960, a new proposal for electrical conductivity made by Little [2], which considers conduction through molecular orbitals, led to the idea of molecular conductors, and many research groups started synthesizing them. Molecular conductors consist of a skeleton organic molecule, which is responsible for donating electrons, associated with an electron acceptor. The first remarkable molecular conductor synthesized was the TTF-TCNQ [3], where TTF is the tetrathiafulvalene donor molecule, and TCNQ, the electron acceptor. In 1979, a group led by K. Bechgaard successfully synthesized a series of conducting molecular salts based on the TMTSF molecule [4, 5], the $(\mathrm{TMTSF})_2X$ family, where TMTSF is the tetramethyltetraselenafulvalene donor molecule and $X$ is a counter-anion with various possible symmetries, exhibiting pronounced 1D characteristics. At the same time, a group led by J. M. Fabre synthesized molecular conductors based on the TMTTF molecule [6], the sulfur analogue of the TMTSF molecule, which is also associated with a counter-anion located at its extremities. In this case, TMTTF refers to the tetramethyltetrathiafulvalene molecule.

In addition to the superconducting phase exhibited by the Fabre-Bechgaard salts, a rich phase diagram was discovered for these materials, revealing a Mott insulating (MI) phase, a charge-ordered (CO) phase, spin-density waves (SDW), antiferromagnetic (AF), and spin-Peierls (SP) ground states [7]. Some of these exotic manifestations of matter are strongly related to the strong electronic correlation effects of these materials and exhibit some degree of ordering [8]. The magnitude of the electrons interaction and the physical properties of these compounds can be altered by decreasing the temperature, applying external hydrostatic pressure, or varying the chemical pressure on the molecules (changing the counter-anion) [7]. Exploring the exhibited phases is important due to the fundamental character of the mechanisms involved in their transitions and stabilization, which can be employed in other areas of Physics.

To achieve and comprehend such fundamental and uncommon changes in matter, strong electron-electron interactions have become a significant research focus in condensed matter Physics. This B. Sc. work is divided into 6 main chapters, following a comprehensive path through the phases diagram as the temperature is reduced. In chapter 2,

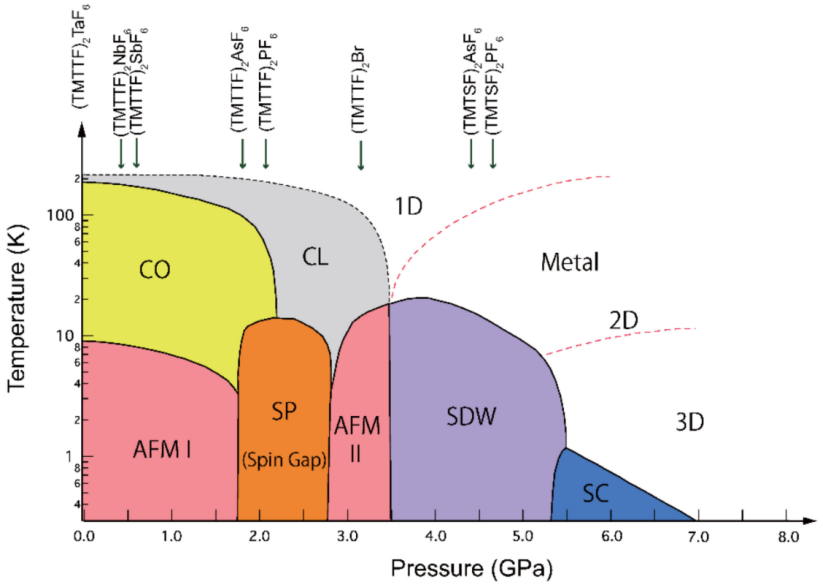


Fig. 1 – Phase diagram showing temperature $T$ *versus* pressure $P$ for the Fabre-Bechgaard salts. The indicated phases are: Mott-insulator, charge-ordered, spin-Peierls, antiferromagnetic, spin-density waves, and superconducting. Systems with different counter-anions are marked by black arrows in the upper part of the diagram [9].

a structural description of the Fabre salts is presented, followed by a brief introduction of the volumetric and uniaxial thermal expansion coefficient and how it evidences phase transitions. In chapter 3, a discussion of the increase in Coulomb repulsion and the localized character of electrons as temperature is decreased is presented. Chapter 4 is dedicated to the charge-ordering phase and ferroelectric phase transitions, which are directly affected by structural defects classified as disorder. In chapter 5, the ordered magnetic ground states are presented, including a brief discussion of the magneto-elastic phase transition, also known as the spin-Peierls phase transition. Chapter 6 contains a detailed description of experimental aspects required to explore low-temperature Physics. Conclusions and perspectives of this work are presented in chapter 7.

## 2 Structural aspects of the Fabre-Bechgaard salts

Molecular conductors like the Fabre-Bechgaard salts are composed of a regular array of quasi-planar organic molecules that form stacks along the $a$-axis, cf. Fig. 2 [10], leading to a preferential overlap of their $\pi$-orbitals in one or two crystallographic directions [11]. Two major aspects of these systems are that their bandwidth is comparable to the energy scale associated with the Coulomb interaction and the rapid change in electronic properties under pressure, due to their soft and compressible lattice, providing a notable coupling of electronic and structural degrees of freedom [12].

The intra-stack interaction occurs in the $b$-axis, and the shortest distance between neighboring molecules is related to the sulfur and selenium neighboring atoms for the Fabre and Bechgaard, respectively [8, 12]. In TMTSF based systems, the shortest distance between stacks is considerably larger when compared to TMTTF based systems. The fact that the overlap between Selenium atoms is larger than the overlap between Sulphur atoms makes the Fabre salts more 1-D than the Bechgaard ones [8].

Six methyl groups located at the molecules extremities form quite symmetrical and soft cavities responsible for lodging the counter-anions, which alternate with TMTTF stacks along the $c^*$-axis cf. Fig. 2 [10, 13]. These counter-anions are related to electrical and structural properties of the Fabre salts, and can be classified by their symmetry: $X$ = $PF_6$, $AsF_6$, and $SbF_6$ (octahedral), Br (spherical) which are centrosymmetrical, and $BF_4$, $ClO_4$, $ReO_4$ (tetrahedral), and SCN (linear), which are not centrosymmetrical [8]. The counter-anions nature is a key factor to these materials, once different species of counter-anions exhibit different sizes and weights, which can affect its mobility inside the cavities, resulting in structural and electrical changes [12,14]. The rotational disorder that counter-anions and methyl groups exhibit at high temperatures is progressively removed upon cooling [8,12]. Due to the counter-anions' arrangement, the dimerization of TMTTF molecules along the stacks is induced, setting the stage for charge-ordering phase transitions, for instance [10]. On average, each dimer has one electron-hole pair, characterizing half-filled band materials, which leads to strong electronic correlation effects like Mott insulators [12].

In these systems, which exhibit metallic behavior at ambient temperature, the strong Coulomb repulsion drives charge localizations at considerably high temperatures, marking a Mott-like metal-insulator phase transition [7]. The localization of these charges is also accompanied by a spin-charge decoupling, leaving the spin degrees of freedom active at low temperatures while the charges remain localized, enabling the establishment of antiferromagnetic or spin-Peierls ground states [7]. More specifically, the Fabre salts exhibit charge localizations and examples of antiferromagnetic and spin-Peierls phases,

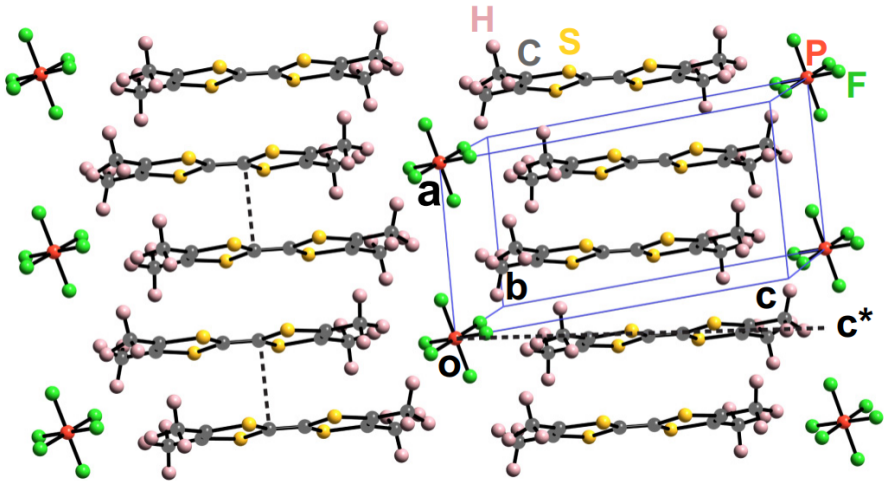


Fig. 2 – Scheme of the $(TMTTF)_2X$ structure with octahedral counter-anions $X = PF_6$. The stacks of TMTTF molecules, which alternate in a "zig-zag" pattern, are along the $a$-axis. The counter-anions, located inside the methyl cavities, alternate with molecule stacks along the $c^*$-axis. Dimers are indicated by the dashed black lines [10].

while the Bechgaard salts exhibit Fermi surface nesting, resulting in a spin-density wave ground state [7]. It is worth mentioning that the magnetic behavior of the metallic phase exhibited by the Fabre salts is described by the Pauli paramagnetism. The latter gives rise to a small magnetization due to the slight increase in the number of spins oriented in a preferential direction once a magnetic field is applied in the system [15].

The Fabre salts are synthesized through an electrochemical process [14, 16], which can be affected by the crystallization of a not well-positioned counter-anion or TMTTF molecule, leading to structural deffects that can affect the electrical properties of these materials, for instance. Dielectric constant measurements as a function of temperature show that the introduction of defects in a system can be enhanced by exposing it to radiation, which leads to changes in physical properties [10].

## 2.1 Phase transitions and thermal expansion measurements

The temperature variation is reflected in systems through their expansion or contraction. This behavior is incorporated into the thermal expansion term [17]. In order to explore it in the context of phase transitions, the volumetric thermal expansion coefficient, which is defined by $\beta$, must be manipulated:

$$\beta(T) = \left(\frac{\partial \ln v}{\partial T}\right)_P, \tag{2.1}$$

$$\beta(T) = \frac{1}{v}\left(\frac{\partial v}{\partial T}\right)_P. \tag{2.2}$$

The isothermal compressibility of solids is defined as [18]:

$$\kappa_T = -\frac{1}{v}\left(\frac{\partial v}{\partial P}\right)_T. \tag{2.3}$$

Now, in order to incorporate Eq. (2.3) in Eq. (2.2), the derivative term in Eq. (2.2) must be decomposed as it follows:

$$\left(\frac{\partial v}{\partial T}\right)_P = \left(\frac{\partial v}{\partial P}\right)_T \left(\frac{\partial P}{\partial T}\right)_v. \tag{2.4}$$

Replacing Eq. (2.4) in Eq. (2.2) gives:

$$\beta(T) = \frac{1}{v}\left(\frac{\partial v}{\partial P}\right)_T \left(\frac{\partial P}{\partial T}\right)_v, \tag{2.5}$$

where the isothermal compressibility term can be easily identified, leading to:

$$\beta(T) = -\kappa_T \left(\frac{\partial P}{\partial T}\right)_v. \tag{2.6}$$

A link between Eq. (2.6) and entropy is established starting from the Helmholtz free energy $F(v, T)$, which is defined as [18]:

$$F = u - TS, \tag{2.7}$$

where $u$ represents the internal energy of the system, and $S$ the entropy. Computing the partial derivatives of Eq. (2.7) results in:

$$\left(\frac{\partial F}{\partial T}\right)_v = -S, \tag{2.8}$$

$$\left(\frac{\partial F}{\partial v}\right)_T = -P. \tag{2.9}$$

By replacing Eq. (2.9) in the volumetric thermal expansion coefficient, Eq. (2.6) turns in:

$$\beta(T) = -\kappa_T \left[\frac{\partial}{\partial T}\left(-\frac{\partial F}{\partial v}\right)_T\right]_v, \tag{2.10}$$

$$\beta(T) = -\kappa_T \frac{\partial^2 F}{\partial T \partial v}. \tag{2.11}$$

Equation (2.8) can now be replaced in Eq. (2.11), resulting in the link between entropy and the volumetric thermal expansion coefficient:

$$\beta(T) = \kappa_T \left(\frac{\partial S}{\partial v}\right)_T . \tag{2.12}$$

In the verge of a phase transition, the entropy of the system suffers a drastic enhancement due to the competition between the phases and between their respective energy scales, usually giving rise to a signature on thermal expansion measurements [19]. In order to explore the individual contributions that constitute the volumetric thermal expansion coefficient, it can be described by the linear thermal expansion coefficients:

$$\beta(T) = \sum_i \alpha_i, \tag{2.13}$$

where $i = a$, $b$, and $c$ are the crystallographic axes and:

$$\alpha_i = \frac{1}{l_i}\left[\frac{\partial l_i(T)}{\partial T}\right]_P , \tag{2.14}$$

where $l_i$ represents the system length in one direction. The equation above is valid for all symmetries in which $a$, $b$, and $c$ are perpendicular to each other [17]. Equation (2.14) provides uniaxial contributions to the volumetric thermal expansion coefficient, which allows the observation of anisotropic effects. In the case of the Fabre salts, the crystal lattice is formed by three different lattice parameters where the angles $\alpha$, $\beta$, and $\gamma$ are also different, classifying a triclinic structure.

## 3 The electrons localization and the emergence of an insulating phase

All the compounds based on TMTTF and TMTSF molecules are metals at room temperature, with electrons fully free to "hop" through the crystal lattice sites. As the temperature decreases, electrons start to lose their hopping capability, localizing themselves in a crystal lattice site due to the competition between hopping and Coulomb repulsion energies [8]. When the Coulomb interaction becomes sufficiently strong, the system undergoes a Mott-like metal-insulator phase transition [8].

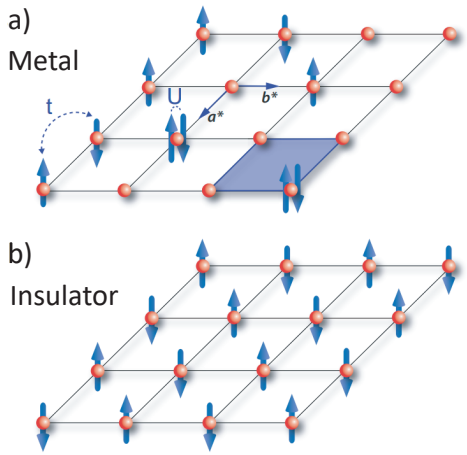


Fig. 3 – a) Scheme of a crystal lattice where itinerant electrons can "hop" from one site to another, indicated by the hopping term $t$, and double occupation is allowed due to low Coulomb interactions $U$. The unit cell of the lattice is highlighted in blue, with vectors $a^*$ and $b^*$. Spins are indicated by the blue arrows. b) Due to strong Coulomb interactions, localized electrons mark a Mott insulating antiferromagnetic phase. Figure adapted from Ref. [20].

Electrons cannot always be treated as free particles due to their interaction with the crystal lattice. This interaction gives rise to the so-called energy bands, which are specific energy spectrums that the electrons can occupy, and are formed by the overlap between atomic orbitals from the periodic crystal lattice [15]. These energy bands are separated by energy gaps that forbid electrons from occupying them, which emerges from the interactions between the conduction electrons and the ions that compose the crystal lattice. According to the band theory, the crystal is classified as a metal if the conduction band is partially filled, and in the case of an insulator, this conduction band would be completely filled, making it impossible for electrons to occupy it [15]. In 1937, the first report of an insulating state being stabilized for a non-complete conduction band material was published [21]. N. F. Mott was responsible for explaining this phenomenom by considering the Coulomb interaction between the electrons, giving rise to the studies on strong electron correlations [22]. In this context, electrons start localizing when the ratio $U/W$ overcomes a critical value, i.e., $U/W \approx 1$, where $U$ represents the on-site Coulomb repulsion and $W$ the bandwidth [15].

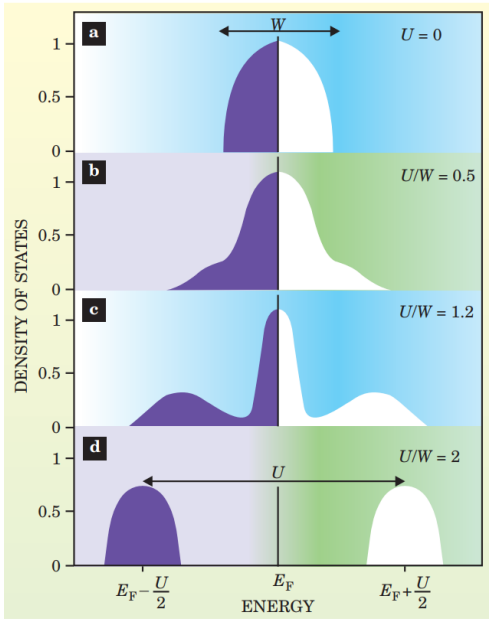


Fig. 4 – Scheme of the evolution of the density of states as $U$ is increased. a) There is no presence of Coulomb interactions, resulting in an elliptical shape of the density of states with its center at the Fermi energy $E_F$. b) Density of states starts to deform due to the presence of a finite value of $U$. c) The deformation of the density of states becomes more drastic as $U$ increases. d) $U$ achives a critical value $(U/W) = 2$, and the density of states is completely separated in two bands with energy $(E_F - U/2)$ and $(E_F + U/2)$. The energy $U$ between the bands indicate the energy cost to doubly occupy a crystal site, energetically favoring the electrons localization. Figure extracted from Ref. [23].

An appropriate model for the comprehension of the electrons' behavior in a Mott metal-insulator phase transition is the so-called Hubbard model [24]:

$$\hat{H} = -\sum_{i,j,\sigma} t_{i,j} a^{\dagger}_{i\sigma} a_{j\sigma} + U \sum_{i} \hat{n}_{i\uparrow} \hat{n}_{i\downarrow}, \tag{3.1}$$

where $t_{i,j}$ is the hopping term, which is associated to the kinetic energy of the electrons "hopping" between crystal sites, $\sigma$ represents the spin projection onto z-axis, $a^{\dagger}_{i\sigma}$ and $a_{j\sigma}$ are, respectively, the creation and annihilation operators that emulate the motion of an electron from one site to another by creating an electron on site $i$ and simultaneously destroying it on site $j$. $\hat{n}_{i\uparrow}$ and $\hat{n}_{i\downarrow}$ are, respectively, the number operators that refer to the number of electrons with spin up and spin down on the same site $i$. At high temperatures, the energy of the system is mostly associated with the hopping term $t_{i,j}$, but decreasing the temperature makes the Coulomb interaction term increase its relevance, making it comparable to $t_{i,j}$, promoting a competition between both energy scales and favoring the electrons localization. The transition temperature $T_{\mathrm{MI}}$ can be enhanced by applying pressure to the system, which brings the crystal sites closer one to another, leading to an increase in Coulomb repulsion [25].

In order to experimentally explore the Mott metal-insulator phase transition, control parameters such as temperature, pressure, and chemical pressure can be changed

[7]. The critical temperature of the transition can be observed through electrical resistivity measurements as a function of temperature, where $\partial\rho/\partial T > 0$ indicates a metallic regime and $\partial\rho/\partial T < 0$ indicates an insulating one [7]. The transition can also be observed through a signature in thermal expansion measurements, as the crystal lattice softens during the transition due to the pronounced reduction in the contribution to the cohesive energy of the crystals made by the electrons when they localize, leading to lattice expansion [19]. In a pressure-induced Mott metal-insulator phase transition, the dynamics of the system undergoes a drastic slowing down due to the formation of metallic puddles in the insulating matrix, characterizing a first-order phase transition [19].

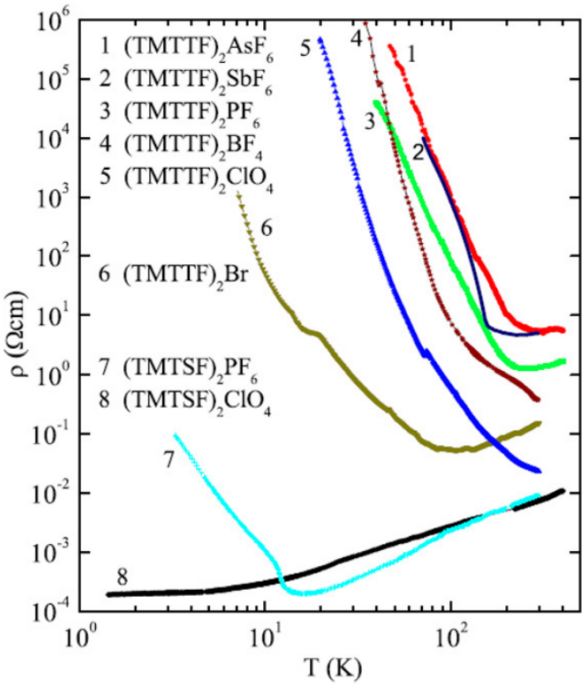


Fig. 5 – Electrical resistivity $\rho$ *versus* $\ln T$ for some Fabre-Bechgaard salts. The change of sign in $\partial\rho/\partial T$ marks the critical temperature $T_{\mathrm{MI}}$ [7].

## 4 The inhomogeneous rearrangement of charges

The Hubbard model provides an excellent approach for systems that exhibit only on-site Coulomb repulsions, but it can be extended to include systems where the inter-site Coulomb repulsion becomes relevant. In this context, the hopping term presented in the standart model exhibited in Eq. (3.1) is distinguished by an intra- and an inter-dimer hopping terms. The extended Hubbard model is defined as [26]:

$$\hat{H} = t_1 \sum_{i\ even,\sigma} (a^{\dagger}_{i\sigma} a_{i+1\sigma} + H.c.) + t_2 \sum_{i\ odd,\sigma} (a^{\dagger}_{i\sigma} a_{i+1\sigma} + H.c.) + U \sum_i \hat{n}_{i\uparrow}\hat{n}_{i\downarrow} + V \sum_i \hat{n}_i \hat{n}_{i+1}, \quad (4.1)$$

where $t_1$ and $t_2$ are, respectively, the intra- and inter-dimer hopping terms, and $V$ represents the first-neighbor Coulomb repulsion, with $\hat{n}_i$ and $\hat{n}_{i+1}$ being the number operators relative to the $i$ and $i+1$ crystal sites. When the inter-site Coulomb repulsion reaches a certain critical value, i.e., when electrons in neighboring sites repell each other more strongly, the reduction of the total electrostatic energy of the system is achieved by the self-rearrangement of the charge carriers, leading to a non-uniform configuration of them, forming a well-defined superstructure also known as a Wigner lattice of localized charges [7, 12, 27]. This is the so-called charge-ordering (CO) phase transition.

The critical value of $V$ can be achieved by decreasing the temperature or applying pressure in the system. Instead of presenting an insulating character, the charge-ordering phase transition does not require an insulating phase above the critical temperature [8]. This is the reason why some systems present a CO phase transition concomitant with a Mott metal-insulator phase transition, as is the case for $(TMTTF)_2SbF_6$, where $T_{\mathrm{CO,\ MI}} \approx 154\,\mathrm{K}$ [8, 29].

Above $T_{CO}$, in the regime where $t_1 >> V$, the electrons are completely able to move from one site to another inside the dimers, maintaining the spin orientation, i.e., $S_Z(1) = S_Z(2) = -S_Z(3) = -S_Z(4)$ [28], where $S_Z(i)$ represents the spin moment at the $i^{th}$ site of the crystal lattice. The charge disproportion ($\pm\delta$) caused by their rearrangement occurs along the molecular chain in a pattern where charge-"rich" ($0.5e^- + \delta$) and charge-"poor" ($0.5e^- - \delta$) sites alternate, i.e., a 1010 pattern, where 1 represents the richer molecule and 0 the poorest [10]. The modulation that marks the charge-ordered phase is usually referred to as a $4\,k_F$ charge-density wave [7], where $k_F$ refers to the Fermi vector. Said ordering corresponds to a real-space charge modulation where the periodicity is twice the distance between the TMTTF molecules along the chain direction, i.e., dimers are composed of one charge-"rich" molecule and one charge-"poor" molecule. When a CO phase transition takes place, the inversion symmetry of the stacks is broken [10]. Simul-

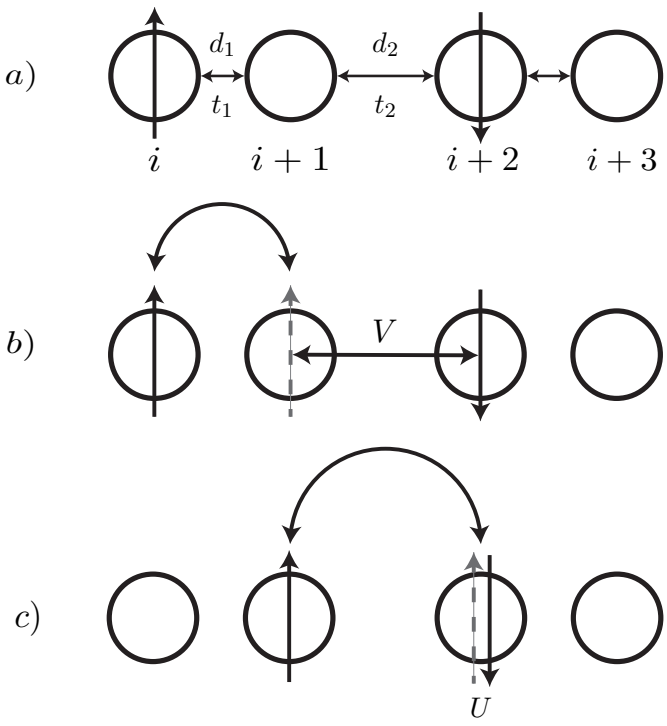


Fig. 6 – Scheme of a quarter-filled dimerized antiferromagnetic spin chain. a) Taking $i = 1$, the pairs 1-2 and 3-4 form dimers, $t_1$ represents the intra-dimer transfer integral and $t_2$ the inter-dimer transfer integral, where $t_1 >> t_2$. b) $V$ represents the inter-site Coulomb interaction. c) $U$ represents the on-site Coulomb repulsion. The arrows indicate electron spins. Figure adapted from [28].

taneously, the transition also breaks the symmetry of the magnetic degrees of freedom, leading to the formation of $S = 1/2$ localized magnetic chains [10, 30].

Once the charges begin to rearrange themselves, electric dipoles start to be formed due to the charge disproportion experienced by the dimers. When the system reaches the critical value $V_C$, the charge-ordered phase is stabilized, and electric dipoles orient themselves in a preferential direction. Therefore, at $T_{CO}$ the system undergoes a concomitant ferroelectric phase transition due to the presence of a finite polarization [31].

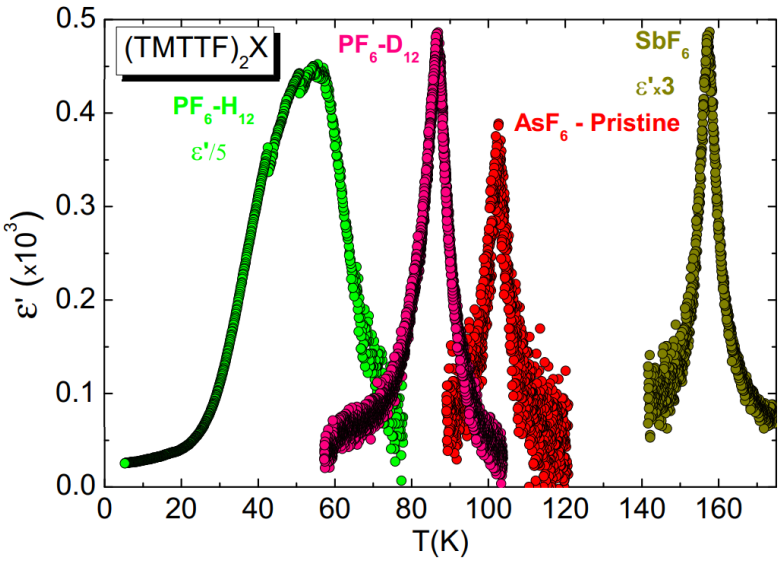


Fig. 7 – Quasi-static (fixed frequency $f = 1\,\mathrm{kHz}$) dielectric constant measured in the $c^*$-axis for the fully hidrogenated and 97.7% deuterated $(TMTTF)_2PF_6$, $PF_6(H_{12})$ and $PF_6(D_{12})$ respectively (green and pink data set), $(TMTTF)_2AsF_6$ (red data set) and $(TMTTF)_2SbF_6$ (dark yellow data set). The peak in the quasi-static dielectric constant indicates a transition to a charge-ordered and a Mott-Hubbard ferroelectric phase [10].

### 4.1 Lattice effects in the charge-ordering phase transition

Different counter-anions show different sizes and weights, which directelly affect $T_{CO}$ due to the change in the free space, and in the pressure inside the cavities, highlighting the lattice effects in the CO phase transition [7]. For $X = PF_6$, $AsF_6$ and $SbF_6$, the respective ferroelectric phase transition temperatures are $\approx 60\,\mathrm{K}$, $100\,\mathrm{K}$, and $155\,\mathrm{K}$ [10, 12]. The deuteration of the systems demonstrates the relevance of the environment created by the cavities, which is related to the degrees of freedom of the counter-anions lodged in it, by increasing $T_{CO}$ in relation to the hydrogenated systems [32], i.e., since the C-D bonds are $\approx 0.01\,\text{Å}$ shorter than the C-H ones [32].

Inside the cavities, the counter-anions present rotational and translational degrees of freedom, which are key ingredients to stabilize the long-range ordering formed below $T_{CO}$ [34]. The translational degrees of freedom can be visualized as two possible configurations of the H-bonds between the anion and its methyl groups [12]. The charge-ordered phase stabilizes due to the fact that the counter-anion may suffer displacements from its inversion center inside the methyl groups cavities, induced by the local electrical field from the charge disproportion [10, 34]. Spectroscopic experiments employing $X = SbF_6$ and $AsF_6$ systems revealed that, below $T_{CO}$, counter-anions interact strongly with the charge-"rich" molecule of the dimer [35, 36].

Uniaxial thermal expansion measurements as a function of temperature are very useful to observe phase transitions due to their intrinsic entropy enhancement [19], which, according to Eq (2.12), is reflected in a signature on the measurements. For the Fa-

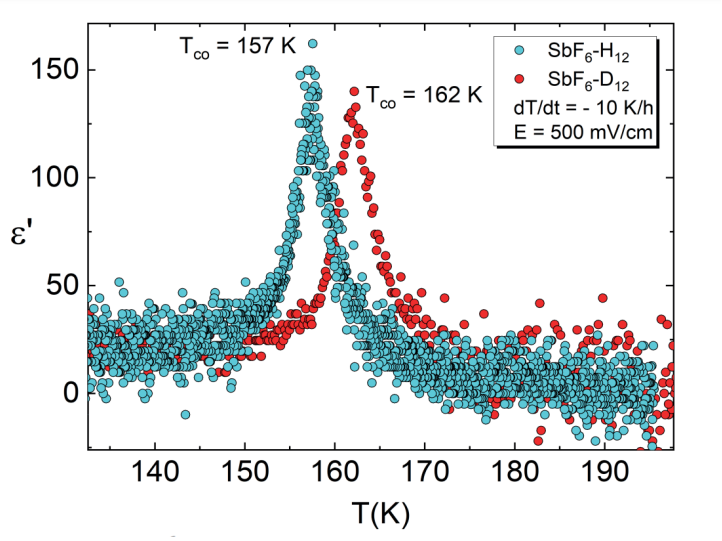


Fig. 8 – Quasi-static dielectric constant $f = 1\,\mathrm{kHz}$ for $(TMTTF)_2SbF_6$. The blue data set indicates the hydrogenated variant ($H_{12}$) and the red data set the deuterated variant ($D_{12}$), with $T_{CO}$ values of 157 K and 162 K, respectively. The employed cooling rate was 10 K/h and an applied electric field of 500 mV/cm [33].

bre salts, uniaxial thermal expansion measurements carry additional information related to the counter-anions mobility [8]. For counter-anions that exhibit octahedral symmetry, rotational degrees of freedom are very active at high temperatures, which is evidenced by a negative slope in thermal expansion measurements, reflecting the decrease in the inter-stacks distances as the temperature is increased [10]. This effect is more pronounced in the $c^*$-axis due to the counter-anions contribution [8]. The saturation in the uniaxial thermal coefficient measurements indicate that counter-anions start loosing their rotational mobility, and at sufficiently low temperatures, the rotational degrees of freedom of the counter-anions completely freeze, losing their rotational motion, turning the slope of uniaxial thermal expansion positive. For $X = SbF_6$, $T_{CO}$ is above the counter-anions rotational degrees of freedom freezing temperature of $\approx 80\,\mathrm{K}$, i.e., the negative slope is present for $T < T_{CO}$, so that the counter-anions are able to collectively change their orientation and stabilize the CO phase. For $X = AsF_6$, $T_{CO}$ is located in the regime around 105 K where the rotational degrees of freedom of the anions just begin to freeze, and for $X = PF_6$ the CO phase transition occurs when the counter-anions are already frozen at $\approx 75\,\mathrm{K}$ [8].

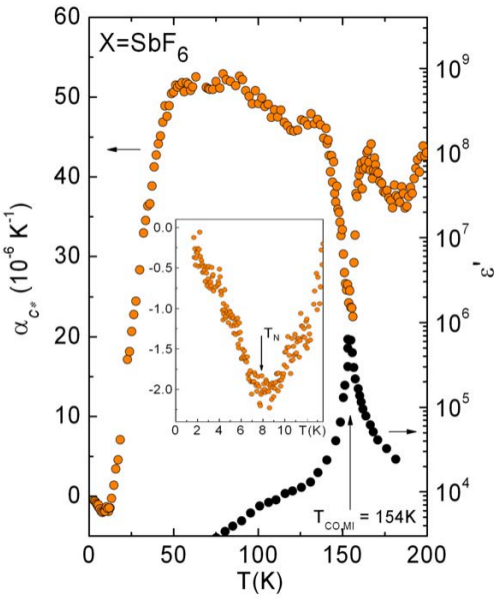


Fig. 9 – Uniaxial thermal expansion coefficient along the $c^*$-axis, $\alpha_{c^*}$ (left axis) and the real part of the dielectric constant, $\varepsilon'$ (right axis) for $(TMTTF)_2SbF_6$. At $T = 154\,K$, the dielectric constant data set (from Ref. [37]) simultaneously show a CO and a Mott metal-insulator phase transition, and concomitantly, the thermal expansion coefficient also presents a signature at this temperature. The inset containing $T_N$ shows a tiny anomaly in $\alpha_{c^*}$ due to antiferromagnetic ordering around 8 K [28].

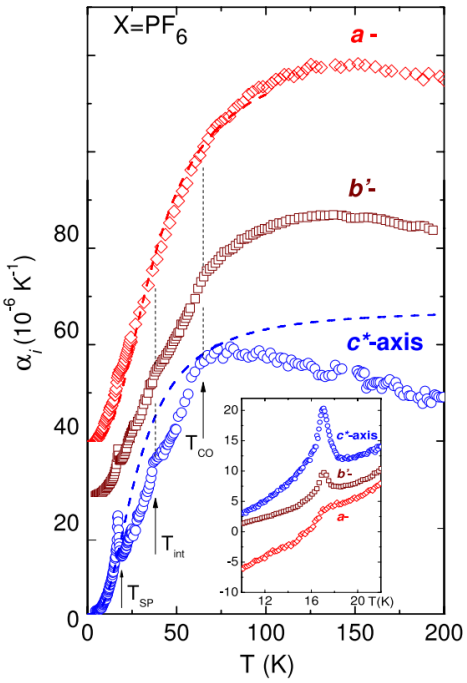


Fig. 10 – Uniaxial thermal expansion coefficient along the $a$-, $b'$-, and $c^*$-axis for $(TMTTF)_2PF_6$. Data are shifted just for clarity. The red dashed line is a Debye fitting up to 100 K. The arrows indicate the temperatures of CO ($T_{CO}$), the intermediary ($T_{int}$) and the spin-Peierls ($T_{SP}$) transitions. The change in the thermal expansion coeffiencient slope indicate the temperature in which the rotational degrees of freedom of the counter-anions freeze, and stop contributing to it. The negative slope is more pronunced in the $c^*$-axis measurements than in the $a$- and $b'$-axis due to the counter-anions contribution, characterizing anisotropic effects [28].

Quasi-static dielectric constant measurements as a function of temperature demonstrate the ferroelectric phase transition, where $T_{CO}$ is located at the maximum value of $\varepsilon'$, the real component of the dielectric constant. Below $T_{CO}$, the dielectric constant values decrease due to the pointing of electric dipoles in a preferential direction. The establishment of ferroelectric phases in the Fabre salts is typically marked by a peak-like transition, which indicates that all the anions undergo collective displacements from their inversion centers [10].

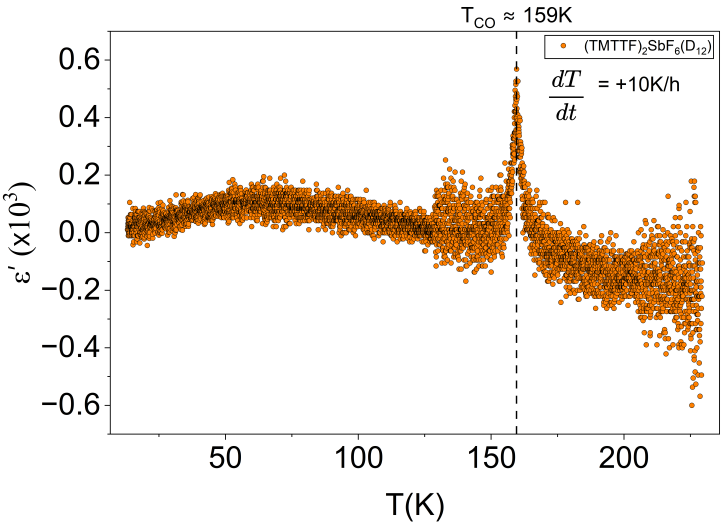


Fig. 11 – Quasi-static dielectric constant for $(TMTTF)_2SbF_6(D_{12})$, where $T_{MI,\,CO} \approx 159\,K$ is indicated by the vertical black dashed line. The peak-like character marks the collective displacement of the counter-anions in order to stabilize the charge disproportion. Negative values refer to the reminiscent metallic phase that this system exhibits at high temperatures. The presented measurements were taken by Prof. Mariano de Souza and Dr. L. Squillante.

If $T_{CO}$ is low enough, the rotational degrees of freedom of the counter-anions freeze before the ferroelectric transition and they cannot undergo the correct displacement to stabilize the charge-ordered phase, creating different ferroelectric domains with different activation energies in the system, changing the peak-like character to a relaxor-like transition, as is the case for $X = PF_6(H_{12})$ [38]. The saturation of the uniaxial thermal expansion coefficient of the system at $\approx 80\,K$ indicates that the rotational degrees of freedom of the counter-anions begin to freeze, and the slope change at $\approx$ 75 - 70 K marks their total freezing, removing its contribution to uniaxial expansion or contractions [8].

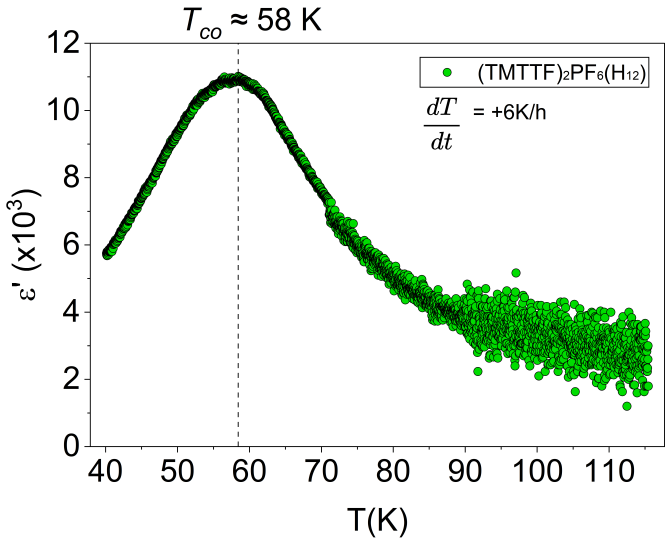


Fig. 12 – Quasi-static dielectric constant for $(TMTTF)_2PF_6(H_{12})$. $T_{CO} \approx 58\,K$ is indicated by the vertical black dashed line. The relaxor-like phase transition is a consequence of ferroelectric puddles in the system. The dispersion of the data above $T_{CO}$ is related to the rotational degrees of freedom of the counter-anions that freezes at $\approx 75\,K$. The presented measurements were taken by Prof. Mariano de Souza and Dr. L. Squillante.

Ferroelectric domains can be classified as disorder in the systems [10], which can take place for two major reasons. In pristine Fabre salts, i.e., not irradiated samples, disorder is easily established by the inversion of a counter-anion orientation [10], which interchanges the positions of charge-"rich" and charge-"poor" molecules along the stack, creating a ferroelectric puddle with opposite polarization. X-ray irradiation breaks both donor molecules and counter-anions [39,40], which changes the electrical balance between dimer and counter-anions, frustrating the long-range ordering by inducing molecular displacements in the surroundings of a defect. The detection of ionized and neutral molecules in irradiated systems through Raman scattering investigations confirmed that the break of the chemical bonds of a donor molecule prevents the coupling of donors into dimers [40], forming the ionized $TMTTF^+$ species. But the break of the chemical bonds of an anion leads to the formation of neutral $TMTTF^0$ species due to the impossibility of transferring one electron from the TMTTF stack to the counter-anion [40]. These factors contribute to the attenuation of the anomaly present in the dielectric constant measurements of irradiated Fabre salts.

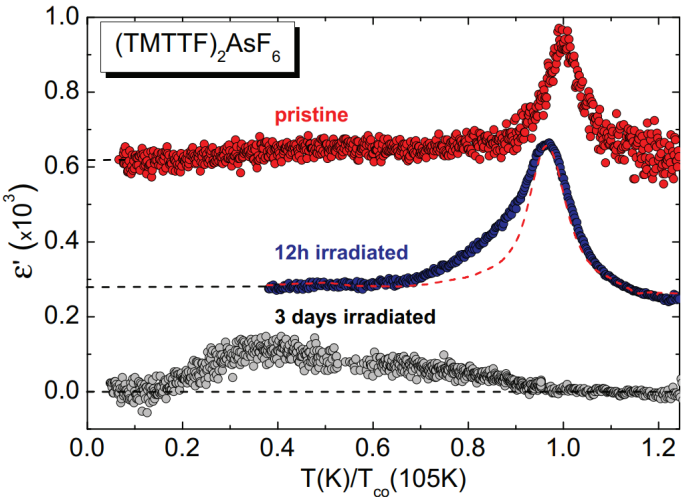


Fig. 13 – Quasi-static dielectric constant for pristine $(TMTTF)_2AsF_6$ (red data set), for 12 h irradiated (blue data set), and three days irradiated (gray data set). The peak-like anomaly is gradually attenuated as the exposure time to X-rays increases. The peak observed for the three days irradiated sample is relative to the Maxwell-Wagner polarization [10].

Quasi-static dielectric constant measurements with $X = AsF_6$ revealed that the anomaly in the dielectric constant is gradually attenuated as the exposure time to X-rays increases [10], until it completely vanishes and only the Maxwell-Wagner polarization between the sample and the layer of carbon conductive paint that covers it can be detected. The attenuation of the anomaly is also caused by damages introduced into the system through the repetition of cooling cycles [10].

# 5 Magnetic ground states of the Fabre salts

One of the ground states of the Fabre salts is the antiferromagnetic phase, which can be observed in two different regions in the phase diagram presented by these systems [7]. This phase is characterized by the anti-alignment of the spins that are associated with the crystal lattice sites, which starts to occur as electron correlations become relevant. To better understand how the spontaneous anti-alignment of spins is energetically favored, considering a Mott-insulator regime, where electrons do not "hop" and exhibit antiferromagnetic ordering, it is possible to write the following Hamiltonian:

$$H = -\frac{1}{2}\sum_{i,j} J_{ij}\vec{S_i}\cdot\vec{S_j} + g\mu_B\vec{B}\cdot\sum_i \vec{S_i}, \tag{5.1}$$

where $\vec{S_i}$ is the spin at the $i^{th}$ site, $\vec{B}$ is the magnetic field applied in the spin system, and $g$ is the $g$-factor, which characterizes how strongly the magnetic moment of a particle is coupled to an external magnetic field. The last term in Eq (5.1), the so-called Zeeman coupling, has a plus sign due to the negative charge of the electrons, resulting in a dipole moment in the opposite direction. The first term, $J_{ij}\vec{S_i}\cdot\vec{S_j}$, is the interaction energy between spin $i$ and spin $j$. The factor of $1/2$ in the first term of the right-hand side of Eq. (5.1) avoids double counting of spins, since the sum counts both $J_{ij}$ and $J_{ji}$.

In the case where $J_{ij} > 0$, the lowest energy state is when spins $i$ and $j$ are aligned, but when $J_{ij} < 0$, the lower energy state turns out to be when the spins are anti-aligned. The energy difference between these two states is called the exchange energy, and correspondingly, $J_{ij}$ is called the exchange constant. As in the case of ferromagnets ($J > 0$), the antiferromagnetic ground states of the Fabre salts take place even in the absence of any applied magnetic field, so that the second term in the right-hand side of Eq. (5.1) can be neglected. The coupling between spins usually drops rapidly as the distance between the spins increases. Therefore, a good model to use is one where only nearest-neighbor spins interact with each other:

$$H = -\frac{1}{2}\sum_{\langle i,j\rangle} J_{ij}\vec{S_i}\cdot\vec{S_j}, \tag{5.2}$$

where the brackets are used to indicate that $i$ and $j$ are nearest-neighbors. In a uniform system in which each spin is coupled to its nearest-neighbors with the same strength, the indices from $J_{ij}$ can be neglected, obtaining the so-called Heisenberg Hamiltonian:

$$H = -\frac{1}{2}J\sum_{\langle i,j\rangle} \vec{S_i}\cdot\vec{S_j}. \tag{5.3}$$

As discussed previously, in the case where $J < 0$, neighboring spins tends to point in opposite directions, and the most natural ordered arrangement is a periodic situation in which alternating spins point in opposite directions. This is what characterizes an antiferromagnetic phase. Such antiferromagnetic systems have zero net magnetization but are magnetically ordered [41].

One-dimensional spin systems have a tendency to order in an antiferromagnetic way. This effect can be observed in the spin susceptibility of the Fabre salts, since at high temperatures, the thermal susceptibility of spins, $\chi(T)$, corresponds to a spin$-1/2$ antiferromagnetic chain, but at significantly low temperatures, the susceptibility decreases because the spins cannot follow the magnetic field anymore [7].

## 5.1 The so-called spin-Peierls transition

The pressurization of an antiferromagnetic system brings the crystal sites closer together, increasing the orbital overlap and the interaction strength $J$. In this scenario, the system tends to minimize its magnetic free energy by forming singlets ($S = 0$), whose energy is lower than the triplets ($S = 1/2$), marking one of the characteristics of a spin-Peierls (SP) transition. In order to counterbalance the magnetic energy reduction due to singlets formation, the lattice concomitantly must distort, i.e., form dimers, and increase the elastic energy of the lattice, which is the second major characteristic of the SP transition, classifying it as a magneto-elastic transition [28, 42–44]. Temperature-dependent susceptibility measurements are a method to detect such transition. The susceptibility of a uniform $S = 1/2$ antiferromagnetic Heisenberg chain has a finite value when the temperature tends to zero. But in a picture where the chain is elastically distorted to form dimers during the SP transition, the susceptibility of the rearranged antiferromagnetic chain goes exponentially to zero as the temperature tends to zero, producing an energy gap in the dispersion relation of this system [32].

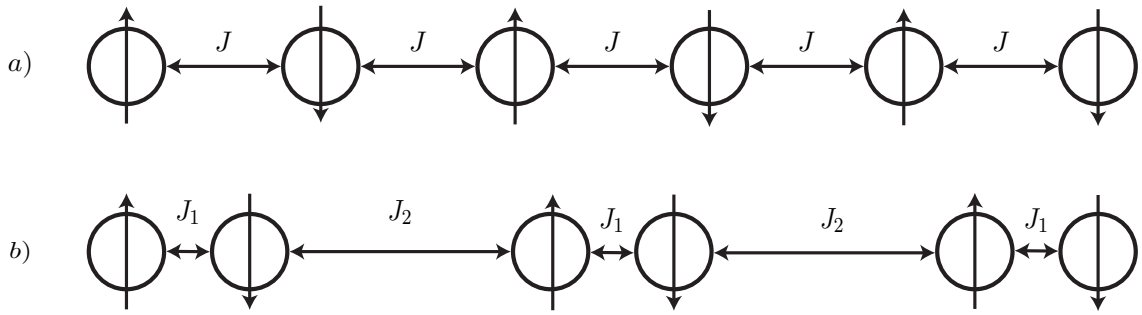


Fig. 14 – Schematic representation of a spin-Peierls transition where the circles are hypothetical lattice sites and the arrows are the electrons spins. a) $S = 1/2$ Heisenberg chain with uniform exchange coupling constant $J$. b) Dimerized chain below $T_{SP}$ with two different exchange coupling constants $J_1$ and $J_2$ representing the intra-dimer and the inter-dimer interactions, respectively. Figure adapted from [28].

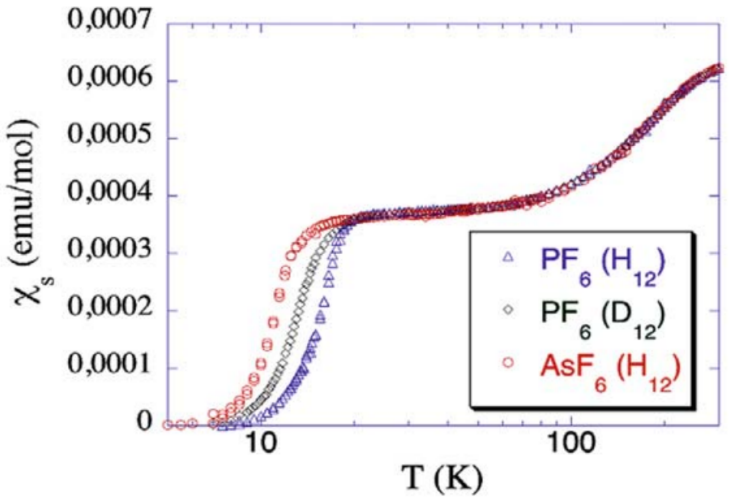


Fig. 15 – SQUID measurements of spin susceptibility, $\chi_S$, of $(TMTTF)_2PF_6(H_{12})$ (blue data set), $(TMTTF)_2PF_6(D_{12})$ (black data set) and $(TMTTF)_2AsF_6(H_{12})$ (red data set) as a function of $\ln T$. $T_{SP}$ is around 16 K, where all three respective susceptibilities start going exponentially to zero [32].

Uniaxial thermal expansion measurements are also a very useful method to observe the spin-Peierls transition, which shows a peak-like anomaly for temperatures usually under 25 K:

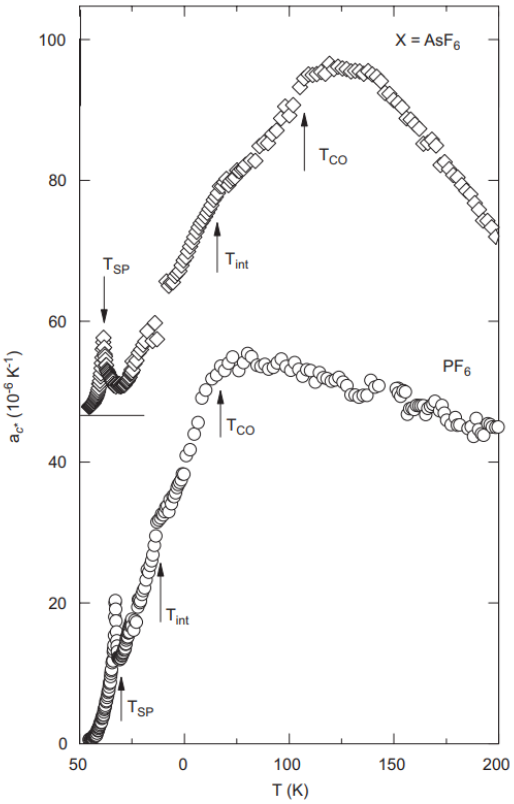


Fig. 16 – Thermal expansion of the $c^*$-axis for $(TMTTF)_2PF_6$ (circles) and for $(TMTTF)_2AsF_6$ (diamonds). The phase transition temperatures $T_{CO}$, $T_{int}$ and $T_{SP}$ are indicated by the arrows [44].

The deuteration of the Fabre salts leads to the decrease of $T_{\mathrm{SP}}$, which shows to be related to the increase of $T_{\mathrm{CO}}$ due to the stabilization of a $4\,k_F$ on-site charge modulation that weakens the $2\,k_F$ bond response, driving the SP instability [32]. An approximate linear relationship of these transition temperatures is presented in Ref. [32], which is:

$$T_{\mathrm{SP}} = 30\,\mathrm{K} - 0.19\,T_{\mathrm{CO}}. \tag{5.4}$$

According to the relationship above, in the absence of a charge-ordered phase, $T_{\mathrm{SP}}$ could be higher than 30K. The expression also shows that $T_{\mathrm{SP}}$ vanishes for $T_{\mathrm{CO}} \approx 160\,\mathrm{K}$, shifting the ground state from spin-Peierls to the antiferromagnetic phase [32], highlighting the lattice effects in the SP phase transition.

# 6 Experimental aspects of low temperature Physics

The Solid State Physics Laboratory, located at UNESP, Rio Claro - São Paulo, and headed by Prof. Mariano de Souza, is equipped with a Teslatron-PT cryostat, capable of achieving temperatures in the range of 1.4 to 300 K and magnetic fields up to 12 T. The cryostat is part of a $^4$He (99.999%) closed cycle, which has a circulation circuit attached to it to continuously cool down the system. The system is equipped with an XDS 10 circulation pump, a SH-110 scroll pump Agilent Technologies, and a HiCube 80 classic turbo pump from Pfeiffer Vacuum. Low temperatures are achieved due to the compression and expansion of $^4$He, which is carried out by an F-70 Sumitomo compressor.

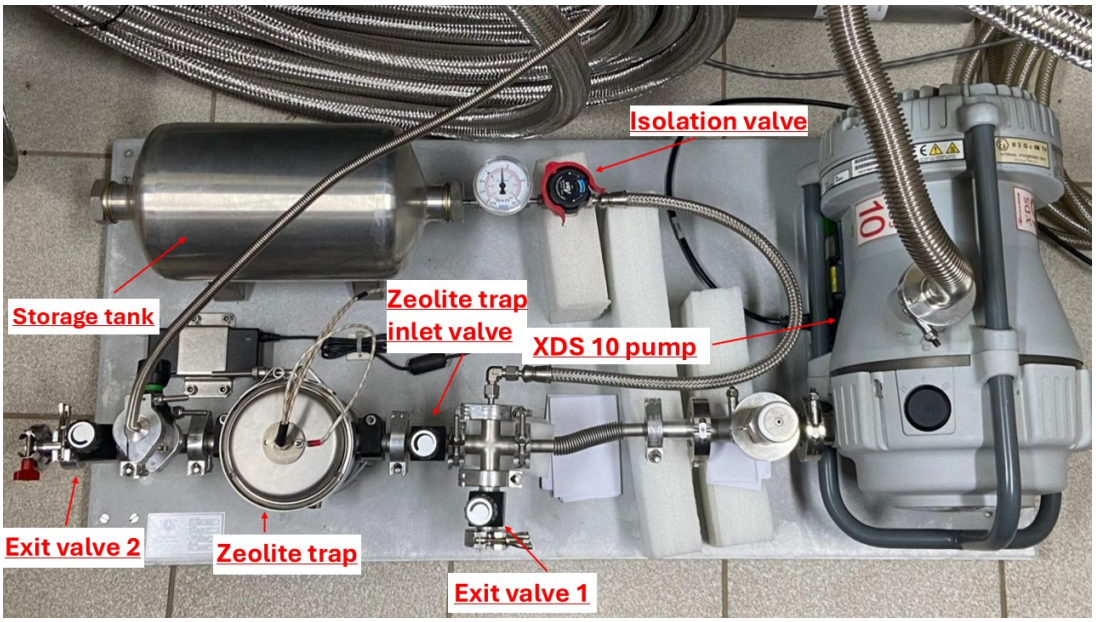


Fig. 17 – Cirulation system containing the storage tank, the isolation valve, exit valves 1 and 2, the zeolite trap and its inlet valve, and the XDS 10 circulation pump.

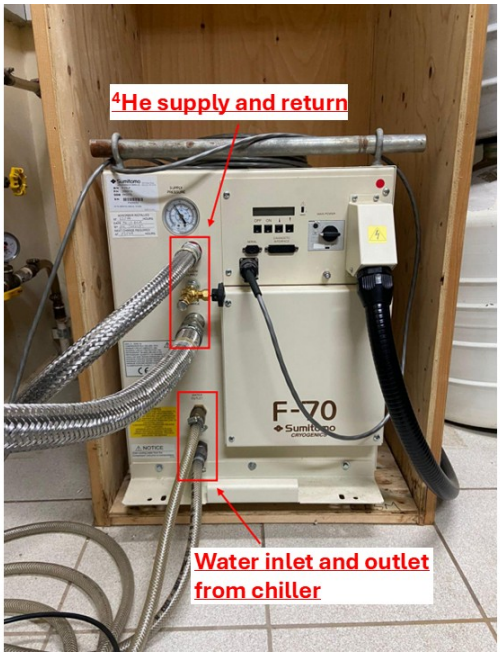


Fig. 18 – F-70 Sumitomo compressor with highlighted $^4$He circulation lines connections and the water inlet and outlet, which enables the cooldown of the compressor during operation.

## 6.1 Cooling by expansion: Teslatron-PT principle of work

The F-70 Sumitomo is responsible for compressing a portion of $^4$He inside its compression chamber. The portion of compressed gas does work, resulting in the decrease of its temperature. Then, the cooled $^4$He is circulated through the closed cycle, i.e., through the cryostat, exchanging heat with the system and then returning warmer to the compressor, where the cycle is continuously repeated. To mathematically understand how $^4$He exchanges heat with its environment, it is necessary to recall the first law of thermodynamics [18]:

$$dQ = du - dw, \tag{6.1}$$

where $Q$ is the amount of heat involved, $u$ is the internal energy and $w$ is the work. Considering that $dw = pdv$, Eq (6.1) can be rewritten as:

$$dQ = du - pdv. \tag{6.2}$$

By analyzing the equation above, it becomes clear that the sign of $dw$ depends on whether work is done on the system or by the system, i.e., $dw < 0$ or $dw > 0$, respectively. If work is done on the gas, its internal energy increases and, consequently, its amount of heat. On the other hand, when the gas freely expands after being compressed, it performs work, decreasing its internal energy and amount of heat, thus cooling the $^4$He. Said process, after $\approx$ 30 - 40 hours, enables the achievement of the base temperature close

to $T = 1.4\,\mathrm{K}$. However, it is necessary to ensure that the circulation system is as clean as possible and that the appropriate vacuum is achieved, in order to avoid gas/system contamination, which can affect the cooling capacity. Therefore, before turning the compressor on, the next steps must be followed.


Fig. 19 – Front view of the Teslatron-PT with both scroll and the turbo pump connected to the system.

## 6.2 Cleaning up of the Zeolite trap and $^4$He circulation lines

The zeolite trap is a device that contains the so-called zeolites, a family of microporous aluminosilicate minerals, responsible for trapping impurities and moisture from gases. The size of the pores exhibited by the zeolites enables the passage of pure gases and retains impurities and water molecules on its surface, acting as a filter.

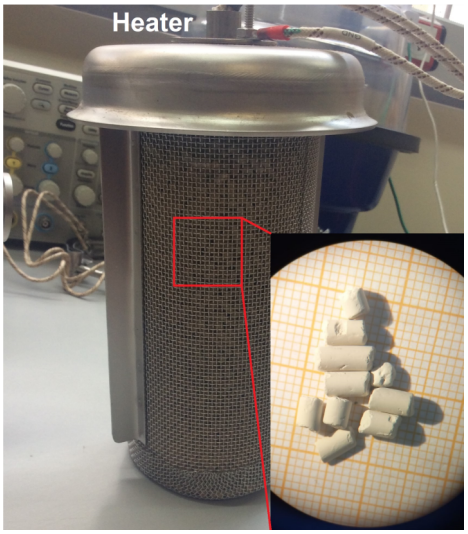


Fig. 20 – Zeolite trap disconnected from the circulation system. The heater is indicated in its upper part. The zeolite crystals are in the lower panel under the microscope view [33].

Successive cycles of $^4$He reduce the adsorption capacity of the zeolite trap, so that keeping it clean is a key factor to maintain the whole system clean. In order to clean the zeolite trap, all the components of the system must be at temperatures above 285 K, and the next procedures must be followed:

*i)* The turbo pump must be connected to the exit valve 2, keeping it closed;

*ii)* The VTI (variable temperature insert) valve and the Zeolite trap inlet valve must be closed;

*iii)* The zeolite trap heater must be turned on for at least one hour. This will promote the degassing of moisture;

*iv)* After one hour, the turbo pump is turned on and the exit valve 2 must be slowly opened;

*v)* With the stabilization of the needle valve pressure close to 0.5 mbar, the exit valve 2 can be closed and the zeolite trap resistance can be turned off.

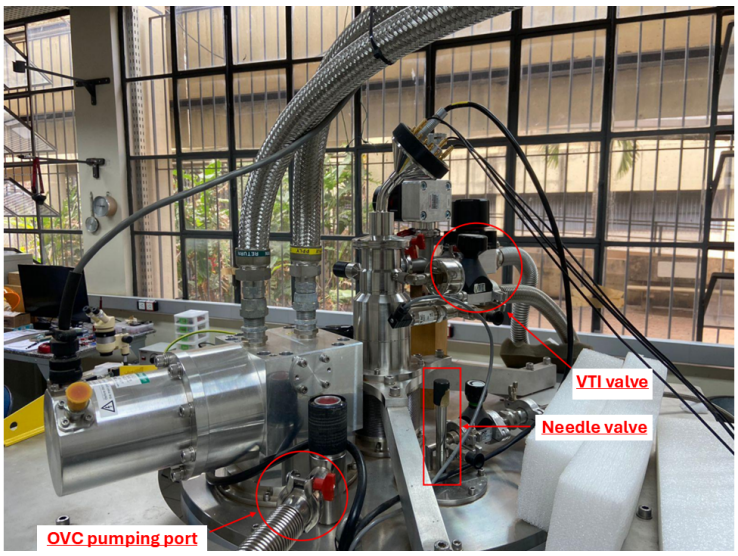


Fig. 21 – Top view of the cryostat with the OVC (outer vacuum chamber) pumping port, the needle valve, and the VTI valve highlighted.

The needle valve pressure is a key indicator of whether the cleaning was successful. The cleaning process ends when the needle valve pressure reaches values under 0.5 mbar, which takes approximately 8 hours.

To ensure the purity of the $^4$He flowing through the circulation lines, they have to be often cleaned. This process is made through the following steps:

*vi)* The scroll pump must be connected to the exit valve 1 with the $^4$He line connected to the $^4$He tank;

*vii)* The needle valve and the VTI valve must be completely opened, and the XDS 10 circulation pump turned on, releasing the $^4$He from the storage tank;

*viii)* The exit valve 1 must be slowly opened to completely remove the $^4$He from the circulation system.

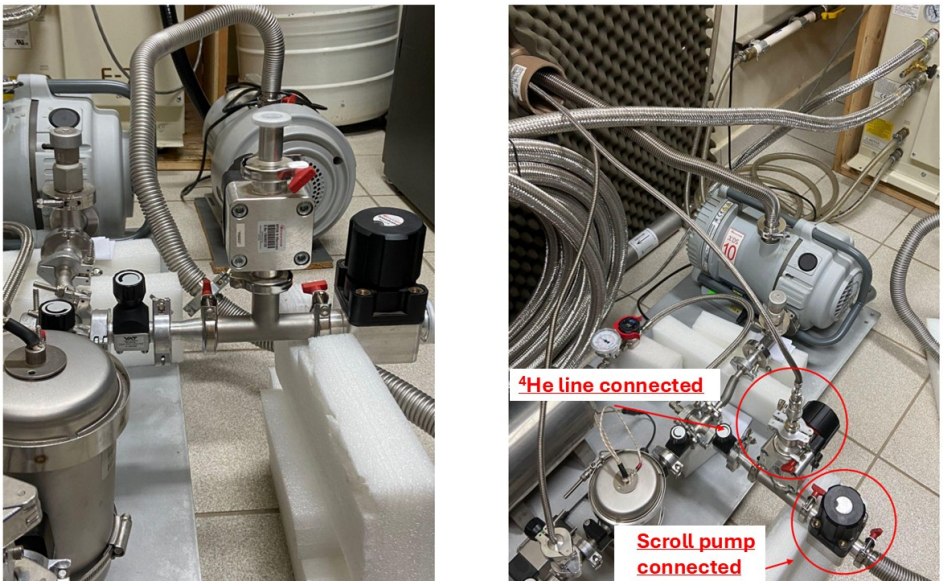


Fig. 22 – a) Adaptor connected to exit valve 1, enabling the simultaneous connection of the $^4$He line and the scroll pump to it. b) Configuration of the circulation system with the $^4$He line and the scroll pump already connected to exit valve 2.

Upon inserting 0.5 mbar of $^4$He in the system and systematically pumping it out 3 to 5 times, it is possible to ensure that the circulation lines are clean. To complete the cleaning process, 0.6 mbar of $^4$He must be inserted in the storage tank, and all the gas present in the circulation system pumped out for a few hours.

In step *iv*, when the exit valve 2 is opened, the needle valve pressure decreases exponentially, which is a prediction made by the so-called continuity equation related to a pumping process, defined by [45]:

$$v dp = G_{tot} dt - S' p dt, \tag{6.3}$$

where $G_{tot}$ is the total portion of gas entering the recipient and $S'$ is the pumping speed. The recipient with fixed volume $v$, which is susceptible to pressure variations $dp$, is described by Eq (6.3) that relates the total portion of gas entering the recipient in a time interval $dt$ and the portion of pumped out gas with a speed $S'$. The zeolite trap is a completely sealed device, so that there is no influx of particles from outside, therefore $G_{tot}$ is zero. Hence, the last equation can be rewritten as:

$$v \frac{dp}{dt} = -S' p, \tag{6.4}$$

which, after a simple manipulation of terms, turns into:

$$\frac{1}{p}dp = -\frac{S'}{v}dt. \tag{6.5}$$

By integrating both sides of the equality:

$$\int_{p_0}^{p} \frac{1}{p}dp = \int_{t_0}^{t} -\frac{S'}{v}dt, \tag{6.6}$$

and by taking $t_0$=0, the following relation can be formulated:

$$\ln(p) - \ln(p_0) = -\frac{S'}{v}t. \tag{6.7}$$

Employing the well-known logarithmic properties, an equation for pressure is easily found:

$$\ln(p) = \ln(p_0) - \frac{S'}{v}t, \tag{6.8}$$

$$e^{\ln(p)} = e^{\ln(p_0)}e^{-\frac{S'}{v}t}, \tag{6.9}$$

$$p = p_0 e^{-\frac{S'}{v}t}. \tag{6.10}$$

Defining the ratio present on the right-hand side of the equation above $-\frac{S'}{v}$ as a characteristic time $\tau$:

$$p = p_0 e^{-\frac{t}{\tau}}. \tag{6.11}$$

The equation above is responsible for describing the exponential decrease of needle valve pressure, which is the case of the zeolite trap cleaning process.

## 6.3 Preparation for system cooling: the circulation of high purity $^4$He

Before the cooling process starts, it is necessary to ensure the homogeneity of the circulating gas, so that the $^4$He must be released from the storage tank and circulated for approximately 12 hours, increasing the cooling efficiency. To achieve these conditions, a few steps must be followed:

*i)* The needle valve must be completely opened by turning it 4 times;

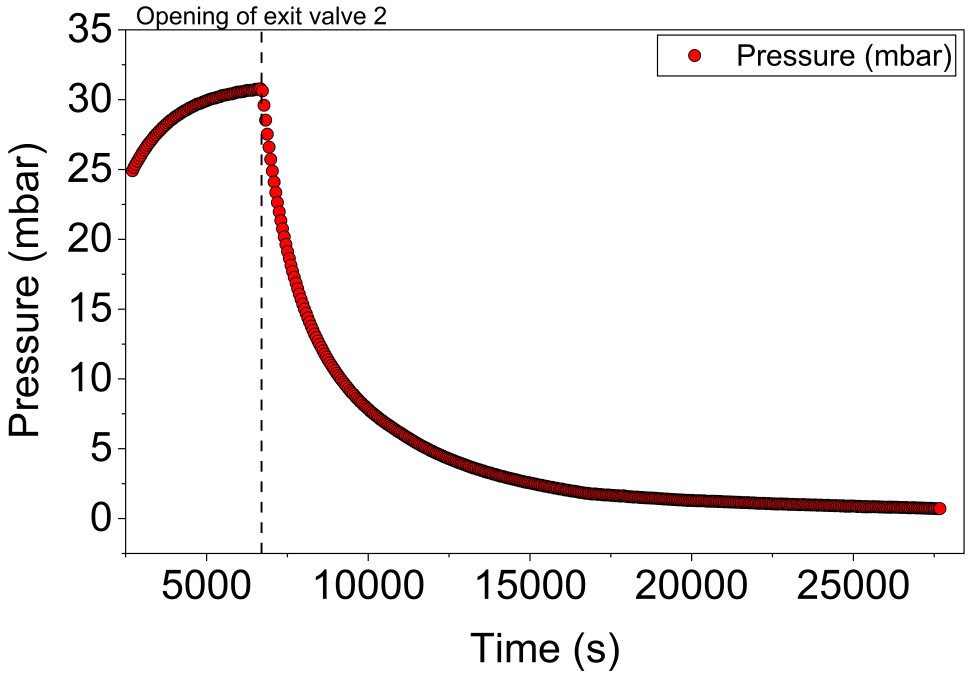


Fig. 23 – Needle valve pressure during the zeolite trap cleaning process. Before the opening of exit valve 2, the pressure increases due to the heating of the zeolite trap in order to increase the cleaning up efficiency. After the opening of exit valve 2, the pressure exhibits an exponential decrease following the relation $p = p_0 e^{-\frac{t}{\tau}}$.

*ii)* The zeoplite trap inlet valve must be completely opened, and then the XDS 10 circulation pump must be turned on;

*iii)* The VTI valve is slowly opened until circulation starts.

In order to finish this process, it is necessary to pump out the OVC and let the gas freely flow for approximately 12 hours.

## 6.4 Decreasing the temperature

Now that the zeolite trap and the circulation lines are cleaned, the system is ready for the start of the cooling process. The compressor is connected to the chiller, which is responsible for cooling the compressor while it operates through a continuous water flow at 17° C. Therefore, the chiller must be turned on at least 15 minutes before starting the compressor. After this, the final steps are:

*i)* The needle valve must be completely closed, and its pressure value must be around 0.0 mbar ± 0.5 mbar;

*ii)* The needle valve must be half a turn opened;

*iii)* The compressor must be turned on.

Once the compressor is turned on, the OVC must be continuously pumped until the pulse tube refrigerator second stage (PT2) reaches temperatures lower than 5 K, which takes about 30 - 40 hours. It is worth mentioning that the circulation system and the compressor are located in a room next to the main location of the laboratory. This support room is constantly cooled by an air-conditioner at 23° C when the compressor is operating.

## 6.5 Adjusting the needle valve pressure

After a few hours of compression, the temperatures of the PT2, the sample space, and the magnet decrease. According to the manuals provided by the Oxford Intruments, the needle valve pressure must be adjusted to 10 mbar when the temperatures of the three cited components converge and stop decreasing ($\approx$ 15 - 5 K). This adjustment must be continuously repeated until the temperature of the components reaches 4 K. Only at this temperature the OVC can be closed and the turbo pump turned off. In order to reach the base temperature of 1.4 K, the needle valve pressure must be adjusted to 5 mbar at this moment.

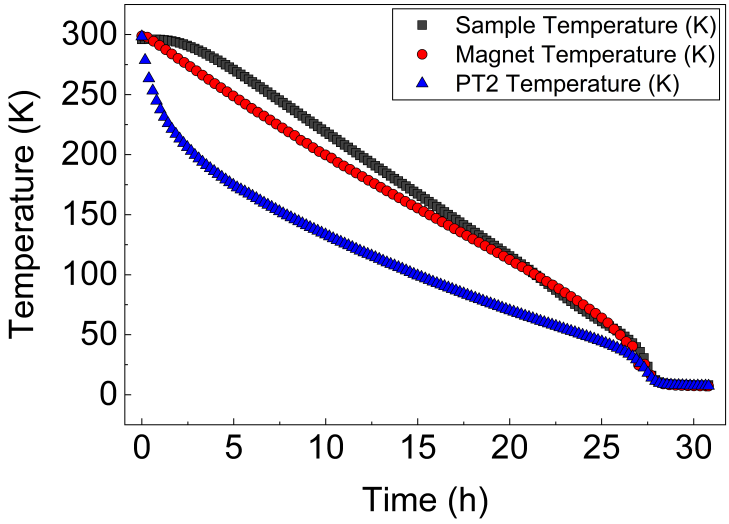


Fig. 24 – Typical behavior of the temperatures of the sample (gray data set), of the magnet (red data set), and of the PT2 (blue data set). After about 28 hours of compression, the temperatures converge and saturate before achieving the base temperature. The needle valve pressure must be ajusted to slightly detach the PT2 from the magnet and the sample space and allow the base temperature achievement.

## 6.6 Attachment of electrical contacts in samples of interest

The preparation of the electrical contacts made in the systems of interest is a very important step for experiments, due to its direct impact on the quality of the collected data. In order to obtain data related to the electrical properties of the Fabre salts, the experiments rely on the emulation of a parallel plate capacitor with the sample,

enabling access to dielectric contributions, for instance. This data are obtained from the relation:

$$C = \frac{\varepsilon' A}{d}, \tag{6.12}$$

where $C$ is the capacitance, $A$ represents the sample area, $d$ the distance between two parallel faces and $\varepsilon'$ the real component of the dielectric constant. Length measures of the chosen system must be taken before starting the process in order to compute the results after the experiment. The capacitance variation embodied on Eq. (6.12) does not discriminate electronic from elastic effects. In order to explore their individual relevance in the phase transitions more specific experiments have to be performed, like electrical resistivity or uniaxial thermal expansion, for instance.

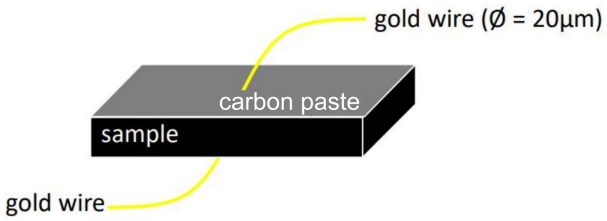


Fig. 25 – Scheme of the sample with the two parallel faces painted with a layer of carbon conductive ink and the tempered gold wires attached to both of them.

Two parallel faces of the system must be covered with a carbon conductive ink, ensuring that there is no contact between both faces, violating the capacitors principle. With the faces uniformly covered, a gold wire with 20 $\mu$m diameter is attached to each face, characterizing the two points method. The dimensions and the fragility exhibited by the Fabre salts turn this step into a very thorough process. In order to develop the required techniques and not damage the systems while preparing their electrical contacts, a series of more resistant systems were prepared before dealing with TMTTF-based ones, employing copper wires.

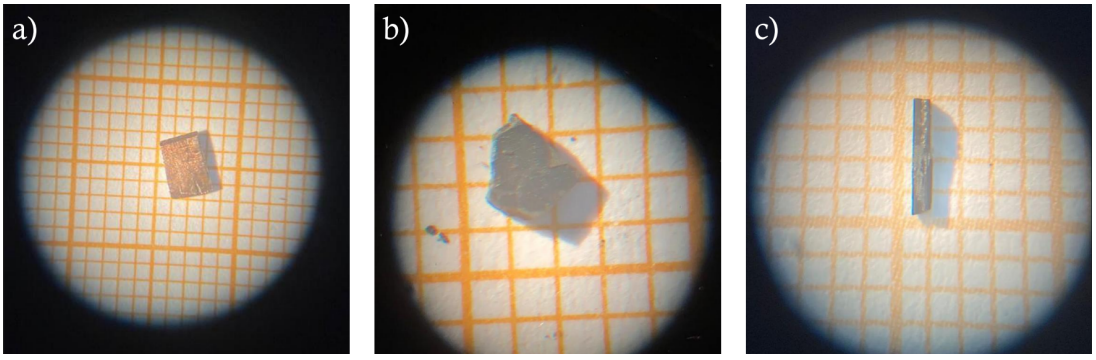


Fig. 26 – a) Copper plate with $(4.0\times3.0\times0.5)\,\mathrm{mm}^3$ and both parallel faces with no cover of carbon paint. b) Sample of $La_2CoMnO_6$ with $(2.0\times2.0\times0.4)\,\mathrm{mm}^3$ with both parallel faces already covered with a layer of carbon paint. This single crystal was provided by Prof. L. Bufaiçal. c) Sample of $(TMTTF)_2PF_6(H_{12})$ with $(3.8\times0.7\times0.2)\,\mathrm{mm}^3$ with no carbon paint in its parallel faces. This single crystal was provided by Prof. J.-P. Pouget and by Prof. P. F. Leylekian.

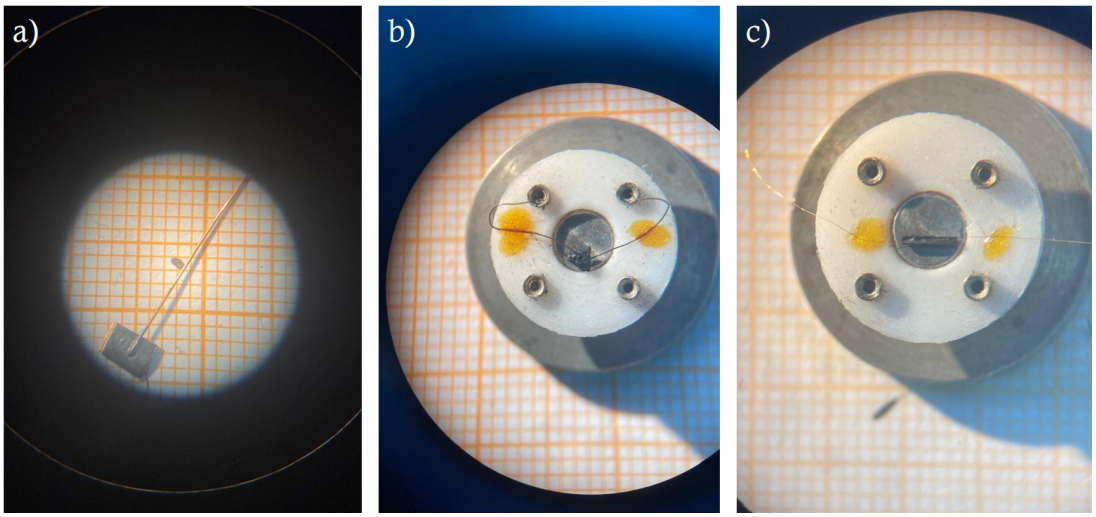


Fig. 27 – a) Sample of copper with both parallel faces covered and a copper wire attached to one of them. b) Sample of $La_2CoMnO_6$ fixed to an insulating mask with both parallel faces covered and copper wires attached to both of them. c) Sample of $(TMTTF)_2PF_6(H_{12})$ fixed to an insulating mask with the parallel faces covered and gold wires attached to both of them.

With the electrical contacts made, the sample must be fixed to an insulating mask, and two drops of a fixing resing proper for low temperatures called Ge Varnish are applyied in order to stabilize the wires. After this, the wires can be introduced in the correct pins of the mask, and the system can now be inserted in the cryostat.

It is worth mentioning that the $La_2CoMnO_6$ was contacted employing copper wires, which transmit a considerable noise to the measurements. Despite not being a molecular conductor, dielectric constant measurements as a function of temperature were also collected for this system, which also exhibits a ordered phase relative to the Co and Mn atoms arrangement [46], and appears to have a ferroelectric transition at high temperatures:

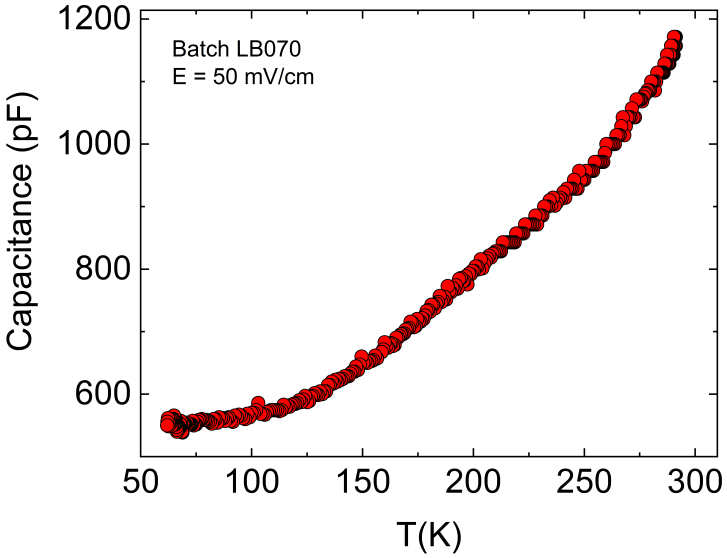


Fig. 28 – Quasi-static dielectric constant of $La_2CoMnO_6$ for a fixed frequency $f$ =1 kHz and electric field $E = 50\,\mathrm{mV\,/\,cm}$.

## 6.7 Achieving high quality vacuum

In order to achieve low temperatures, it is crucial to ensure that the $^4$He (99.999%) remains pure during the cooling process, i.e., the circulation lines must be free of atmospheric air and/or impurities. By pumping out the lines, the system becomes ready to receive the $^4$He and start its operation. This evacuation process is carried out by vacuum pumps that remove almost every unwelcome particles from the system. In the Solid Physics State Laboratory, high quality vacuum is achieved using two vacuum pumps: a SH-100 Agilent Technologies scroll pump and a HiCube 80 classic Pfeiffer Vacuum turbo pump. While there are various types of vacuum pumps with different engineering and functionalities, their basic principles of operation are quite similar.

### 6.7.1 On the principle of work of vacuum pumps

Generally, vacuum pumps are composed of two main stages: the chamber that lodges the copper coils and the chamber that lodges the compressors. A shaft located in the center of the pump connects these two chambers and drives the compressor. When the pump is turned on, an electric current passes through the copper coils, generating out of phase magnetic fields. These magnetic fields affect the rotor, causing it to spin, turning also the shaft. The compressor has an inlet connection for connecting the system to be evacuated and an outlet that vents the impurities evacuated from the system to the atmosphere. In its center, it exhibits the compression chamber and the compressing rotor, which is eccentrically located in relation to the compression chamber. The shaft that rotates due to magnetic fields extends to the center of the compression rotor, which follows the shaft rotation. The compression rotor shows two opposite spring-loaded vanes.

The vanes are continuously pushed against the compression chamber walls due to the extension of the springs, creating two individual environments that trap the extracted gas.

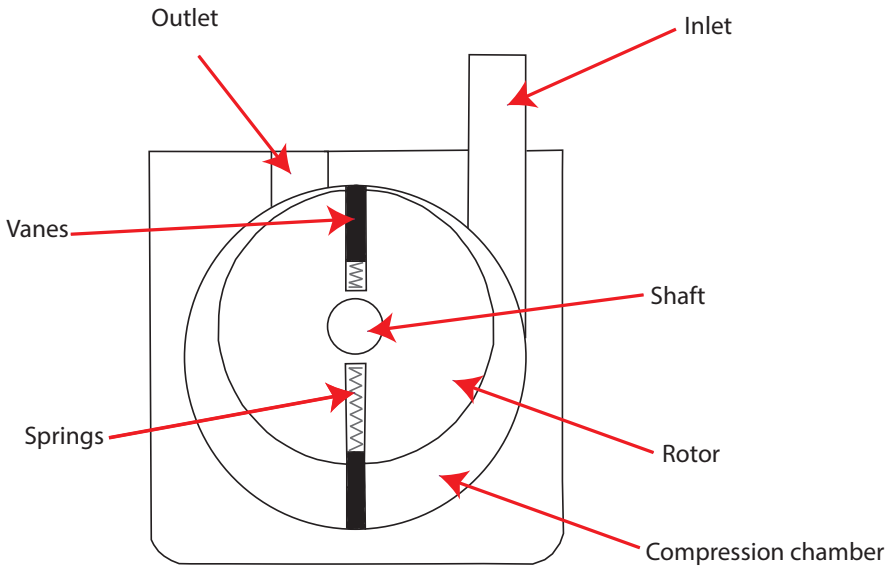


Fig. 29 – Structural view of the compression chamber. The rotating rotor and shaft are eccentrically located in relation to the chamber. Individual cavities are created by the vanes, which are pushed against the chamber walls by springs. The inlet and outlet are located at the upper part of the chamber.

When the system that is going to be evacuated is connected to the vacuum pump, the compression chamber becomes part of the system. As the vanes rotate inside the chamber, the volume of the system increases, generating a lower-pressure zone. A portion of gas from this lower pressure region is then trapped in the compression chamber by the vanes. As the vanes continue to rotate, the portion of trapped gas reaches the outlet and starts to be compressed due to the decrease in available volume, creating a high-pressure region inside the compression chamber. When this pressure exceeds a critical value, the portion of trapped gas leaves the system and goes into the atmosphere. The repetition of this cycle decreases the amount of impurities in the system and its pressure. Usually, in order to increase the pumping capacity, mechanical pumps have more than one compression chamber, i.e., the outlet of one compression chamber is immediately connected to the inlet of another chamber.

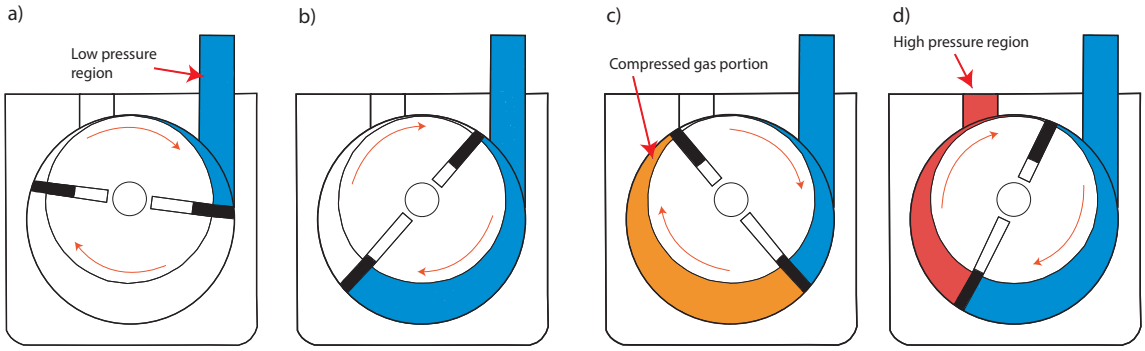


Fig. 30 – Scheme of the principle of work of mechanical pumps. a) The moving vane passes by the inlet and creates a lower-pressure region as it expands the volume of this environment with its rotation. b) The lower pressure region continues to expand until the second vane passes by the inlet. c) When the second vane passes the inlet, then a portion is trapped in the environment created between the vanes, while another lower-pressure region is created in the other environment. d) When the first vane reaches the outlet, the gas starts to be compressed, creating a high pressure region. When this pressure exceeds a critical value, the portion of evacuated gas leaves the system. By repeating this cycle, the system is continuously pumped out, decreasing its internal pressure.

This characterizes the most common vacuum pumps, which are known as mechanical pumps. The sealing between the vanes and the compression chamber walls is ensured by the application of appropriate oil, which can eventually contaminate the system with particles, making it unsuitable for low temperature experiments. To maintain a contamination-free system during the pumping process, a SH-110 scroll dry pump is used to reduce the pressure. When dealing with scroll pumps, the process of removing portions of air from the system is quite similar to that exhibited by the mechanical pumps, but in order to present a rotating rotor eccentrically positioned inside the compression chamber, scroll pumps exhibit two spiral-shaped scrolls inside the compression chamber, with one being fixed and the other orbiting it.

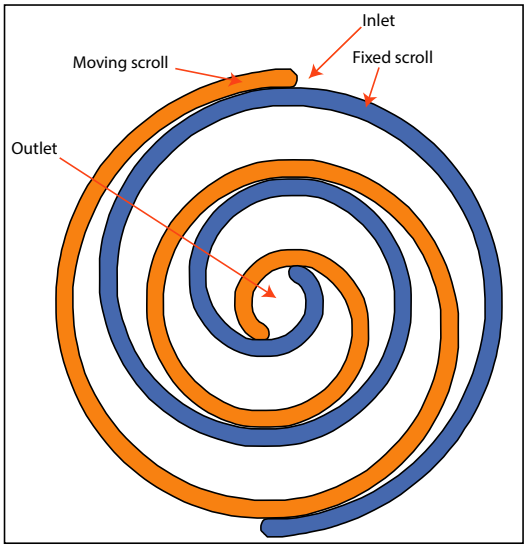


Fig. 31 – Scheme of a scroll pump compressor which is composed of two spiral-shaped scrolls. The blue scroll is fixed while the orange one orbits it in a rotational motion that creates lower pressure pockets inside this structure. The volume of these pockets gradually becomes smaller as they approach the center, where the outlet is located, compressing the evacuated gas.

The rotational motion that one scroll exhibit creates low pressure pockets between the scroll's walls, with the volume gradually decreasing as is approaches the center. The gas pumped from the system is carried through these pockets until it exits the system when a critical pressure is reached in the center of the compressor.

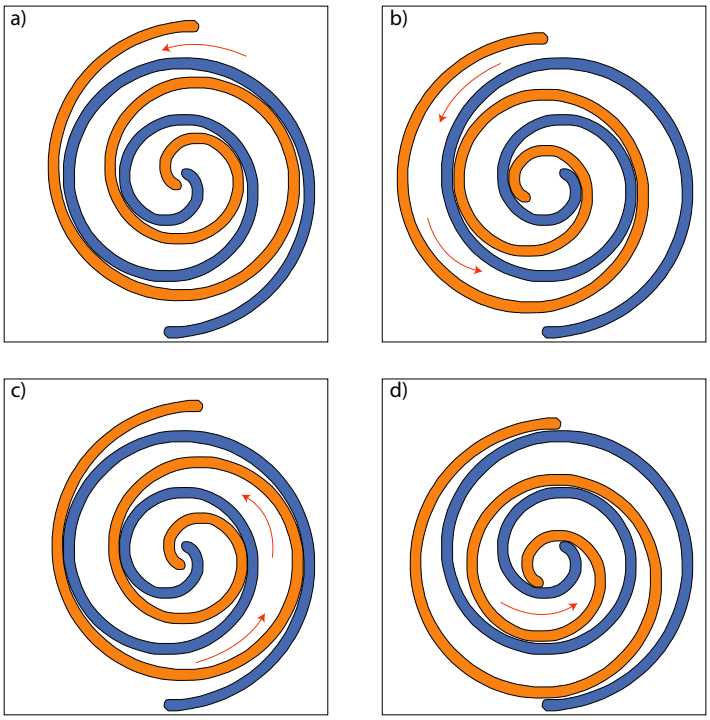


Fig. 32 – Visualization of the rotational motion performed by the orange scroll. The red arrows indicate the flow of evacuated gas inside the lower pressure regions that emerge with this motion.

The Solid State Physics Laboratory is equipped with a scroll pump responsible for pumping the larger portions of gas in the cryostat circulation system. However, the pressures it achieves is still not low enough for performing low temperature experiments. At this point, turbo pumps are required to achieve the proper pressures.

Fig. 33 – Lateral view of the SH-110 scroll dry pump present in the Solid Physics State Laboratory.

In order to produce high quality vacuum, the system cannot be pumped only by the scroll pump due to its limiting capacity. An additional pumping process is employed using a turbo pump, which can achieve much lower pressures compared to the scroll pump. Turbo pumps do not operate at atmospheric pressure due to the large amount of air present in this situation, which could damage the turbo pump. Therefore, it is crucial to ensure that the volume to be pumped with a turbo pump is appropriate for it. The mechanism behind turbo pumps relies on a series of turbines spinning at high speeds. The turbines consists of layers of angled blades spinning in opposite directions, creating an air flow when they spin. The molecules present in the system are attracted by the air flow and "collected" by the angled blades, and then leaves the system. The outlet of the turbines is directly connected to the inlet of a backing mechanical pump, which is responsible for enhancing the turbo pump performance.

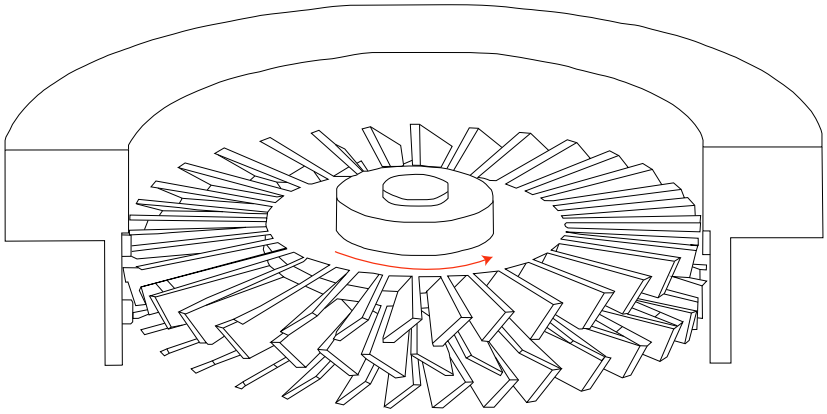

Fig. 34 – Scheme of a generic series of turbines exhibited by turbo molecular pumps. The angled blades are a key factor in trapping the molecules and evacuating them from the system with the air flow created by the rotational motion of the turbines.

The Solid State Physics Laboratory is equipped with a HiCube 80 classic turbo pump from Pfeiffer Vacuum, which is responsible for achieving the required pressures for low temperature experiments. It is frequently employed in the cleaning process and for pumping the OVC during experiments.


Fig. 35 – Front view of the HiCube 80 classic turbo pump present in the Solid State Physics Laboratory.

Unfortunately, the experiments are often interrupted by power losses, which are very critical to the system due to a peculiarity of the turbo pump. When the energy turns off and the turbines stop spinning, the turbo pump ventilates, which would contaminate the system with atmospheric air. A solenoid valve was attached to the turbo pump inlet in order to prevent contamination caused by ventilation. When power goes off, the solenoid valve closes the access to the circulation line and the ventilation occurs

outside the system. However, when power comes back and the solenoid valve is energized, it could open the access to the circulation line before the turbo pump initiates its pumping, and that would contaminate the system. Therefore, Prof. Mariano de Souza and Dr. Lucas Squillante developed an electrical system that only energizes the solenoid valve manually when the circuit is closed. In this context, the turbo pump can be initiated before energizing the solenoid valve, keeping the system clean.

# 7 Conclusions and outlooks

In this B. Sc. work, a brief literature review about strong electronic correlations in molecular systems, especially the exotic phases of matter exhibited by the Fabre salts, as the Mott-insulating phase, the charge-ordered phase, and the magnetic ground states was presented. The description of the structural aspects of the Fabre salts and how they affect the transitions between the mentioned phases, as the disorder effects in the ferroelectric transition, for instance, is also presented. To properly understand the behavior of the electrons as the control parameters are varied, the Hubbard model and its extended version were employed. The Heisenberg Hamiltonian was used to analyze the ordered magnetic ground states. An experimental section was dedicated to the complete description of the steps required to explore electron correlation effects at low temperatures, as the preparation of the systems of interest. Measurements of the dielectric constant of $La_2CoMnO_6$ were obtained and are also presented in the experimental section of this work, which concludes with a description of the principle of operation of different types of vacuum pumps, a crucial aspect for performing low temperature experiments employing $^4$He (99.999%). The perspective of this B. Sc. work is the continuation of studies related to strong electronic correlation effects and a broader experimental exploration of molecular conductors.

## References


1 H. K. Onnes, Proc. K. Ned. Akad. Wet. **14**, 113 (1911).

2 W. A. Little, Phys. Rev. A. **134**, 1416 (1964).

3 F. Wudl, G.M. Smith, E.J. Hufnagel, J. Chem. Soc. Chem. Commun. 1453 (1970).

4 K. Bechgaard, C.S. Jacobsen, K. Mortensen, H.J. Pedersen, N. Thorup, Solid State Commun. **33**, 1119 (1979).

5 D. Jérome, A. Mazaud, M. Ribault, K. Bechgaard, J. Phys. Lett. **41**, 95 (1980).

6 J. L. Galigne, B. Liautard, S. Peytavin, G. Brun, M. Maurin, J. M. Fabre, E. Torrielles, L. Giral, Struct. Sci. **35**, 1129 (1979).

7 M. Dressel, *Naturwissenschaften* **94**, 527 (2007).

8 M. de Souza, J. P. Pouget, J. Phys. Condens. Matter **25**, 343201 (2013).

9 M. Itoi, T. Nakamura, Y. Uwatoko, Mat. **15**, 4638 (2022).

10 M. de Souza, L. Squillante, C. Sônego, P, Menegasso, P. F. Leylekian, J. P. Pouget, Phys. Rev. B **97**, 045122, (2018).

11 K. Yoshizawa, Acc. Chem. Res. **45**, 1612 (2012).

12 J.-P. Pouget, Cryst. **2**, 466 (2012).

13 T. J. Kistenmacher, Solid State Commun. **51**, 931 (1984).

14 R. Rösslhuber, E. Rose, T, Ivek, A. Pustgow, T. Breier, M. Geiger, K. Schrem, G. Untereiner, M. Dressel, Cryst. **8**, 121 (2018).

15 C. Kittel, P. McEuen, Introduction to Solid State Physiscs (2018).

16 M. Formigue, J. Mat. Chem. C **9**, 10557 (2021).

17 T. H. K. Barron, J. G. Collins, G. K. White, Advances in Physics **29**, 609 (1980).

18 A. L Wasserman, Thermal Physics: Concepts and Practice (Cambridge University Press, 2011).

19 I. F. Mello, L. Squillante, G. O. Gomes, A. C. Seridonio, M. de Souza, J. Appl. Phys. **128**, 225102 (2020).

20 L. Squillante, S. Soares, E. Marinho, A. R. Rocha, M. Figueira, A. Seridonio, M. de Souza, Uma introdução compreensiva sobre fenômenos eletrônicos fortemente correlacionados. (2025). Em SciELO Preprints. https://doi.org/10.1590/SciELOPreprints.12120 (Original work published 2025)

21 J. de Boer, E. JW. Verwey, Proc. Phys. Soc. **49**, 59 (1937).

22 N. F. Mott, Proc. Phys. Soc. A **62**, 416 (1949).

23 G. Kotliar, D. Vollhardt, Physics Today **57**, 53 (2004).

24 J. Hubbard, Proc. Roy. Soc. A **276**, 238 (1963).

25 A. Pashkin, M. Dressel, C. A. Kuntscher, Phys. Rev. B **74**, 165118 (2006).

26 H. Seo and H. Fukuyama, J. Phys. Soc. Jpn. **66**, 1249 (1997).

27 H. Seo, J. Merino, H. Yoshioka, M. Ogata, Journal of the Physical Society of Japan **75**, 051009 (2006).

28 M. de Souza, Thermal expansion and transport properties of low-dimensional organic conductors, Phys. Uni. Frankfurt (2008).

29 R. Laversanne, C. Coulon, B. Gallois, J.-P. Pouget, R. Moret, J. Phys. Lett. **45**, 393 (1984).

30 S. Yasin, B. Salameh, E. Rose, M. Dumm, H.-A. Krug von Nidda, A. Loidl, M. Ozerov, G. Untereiner, L. Montgomery, M. Dressel, Phys. Rev. B **85**, 144428 (2012).

31 P. Monceau, F. Y. Nad, S. Brazovskii, Phys. Rev. Let. **86**, 4080 (2001).

32 J. P. Pouget, P. Foury-Leylekian, D. L. Bolloch, B. Hennion, S. Ravy, C. Coulon, V. Cardoso, A. Moradpour, J. Low Temp. Phys. **142**, 147-152 (2006).

33 L. Squillante, The Gruneisen parameter applied to critical phenomena and experimental investigations of correlated phenomena in molecular conductors, 2023 Doctoral Thesis São Paulo State University, Brazil (https://repositorio.unesp.br/entities/publication/4641c05a-2bd7-46b9-b1aa-53d1025f4410).

34 S. Brazovskii, Synth. Metals **133**, 301 (2003).

35 K. Medjanik, M. de Souza, D. Kutnyakhov, A. Gloskovskii, J. Muller, M. Lang, J. -P. Pouget, P. Foury-Leylekian, A. Moradpour, H. -J. Elmers *et al.*, Eur. Phys. J. B **87**, 256 (2014).

36 K. Medjanik, A. Chernenkaya, S. A. Nepijko, G. Ohrwall, P. Foury-Leylekian, P. Alemany, E. Canadell, G. Schonhense, J. -P. Pouget, Phys. Chem. Chem. Phys. **17**, 19202 (2015).

37 F. Nad, P. Monceau, J. Phys. Soc. Jpn. **75**, 051005 (2006).

38 F. Nad, P. Monceau, C. Carcel, J. M. Fabre, Phys. Rev. B **62**, 1753 (2000).

39 C. Coulon, P. Foury-Leylekian, J. M. Fabre, J.-P. Pouget, Eur. Phys. J. B **88**, 85 (2015).

40 R. Swietlik, B. Barszcz, A. Pustogow, M. Dressel, Phys. Rev. B **95**, 085205 (2017).

41 S. H. Simon, The Oxford Solid State Basiscs (2013).

42 J. P. Pouget, R. Moret, R. Comes, K. Bechgaard, J. M. Fabre, L. Giral, Mol. Cryst. Liq. Cryst. **79**, 485 (1982).

43 J. C. Slater, Phys. Rev. **82**, 538 (1951).

44 M. de Souza, A. Bruhl, J. Muller, P. Foury-Leylekian, A. Moradpour, J. P. Pouget, M. Lang, Phys. B: Cond. Matt. **404**, 494 (2009).

45 I. Bello, Vacuum and ultravacuum: Physics and technology (CRC Press, 2018).

46 R. X. Silva, A. S. Menezes, R. M. Almeida, R. L. Moreira, R. Paniago, X. Marti, H. Reichvola, M. Mariško, M. V. S. Rezende, C. W. A. Paschoal, J. Alloys Compd. **661**, 541 (2016).